Modelling and
Simulation in Materials
Science and
Engineering

PAPER • **OPEN ACCESS**

Comparative analysis of diffusive molecular dynamics and traditional molecular dynamics in palladium hydride

To cite this article: Philipp M Schäfer and Christian J Cyron 2026 *Modelling Simul. Mater. Sci. Eng.* **34** 055001

Modelling and Simulation in Materials Science and Engineering

PAPER

OPEN ACCESS

RECEIVED
11 November 2025

REVISED
9 April 2026

ACCEPTED FOR PUBLICATION
11 May 2026

PUBLISHED
17 June 2026

Comparative analysis of diffusive molecular dynamics and traditional molecular dynamics in palladium hydride

Philipp M Schäfer[1,2] **and Christian J Cyron**[1,2,*]

[1] Institute for Continuum and Material Mechanics, Hamburg University of Technology, Eißendorfer Straße 42, 21073 Hamburg, Germany
[2] Institute of Material Systems Modeling, Helmholtz-Zentrum Hereon, Max–Planck-Straße 1, 21502 Geesthacht, Germany
[*] Author to whom any correspondence should be addressed.

E-mail: christian.cyron@hereon.de

Keywords: diffusive molecular dynamics, palladium hydride, long-time atomistic simulation/time-scale bridging, non-equilibrium statistical mechanics, mean-field approximation

Abstract

Diffusive processes on the nanoscale, characterized by coupled diffusion and deformation, pose significant challenges for the assessment using conventional simulation methods due to their long time scales. Diffusive molecular dynamics (DMD) models such diffusive processes by optimizing positions and vibration frequencies of atom sites with variable concentrations evolving based on kinetic equations. Despite its various applications, validation studies for this method still remain limited due to a lack of suitable reference solutions and an absence of comparisons among different kinetic equations. This paper aims to fill these gaps by directly comparing DMD, utilizing different kinetic equations, with traditional molecular dynamics (MD) for the case of palladium hydride on thermal and diffusive time scales. Employing the same interatomic potential in both methods helps to isolate errors attributed solely to the assumptions inherent in DMD. The simulations conducted, which include measurements of lattice and elastic constants as well as surface diffusion and hydration processes of a nanocube, reveal that although DMD generally captures the trends observed in the reference solutions quite well, it exhibits non-negligible quantitative discrepancies in both static properties and diffusive behaviors. Among the tested kinetic equations, a linear approach and a master equation depending on vacancy formation energy showed the best agreement with the reference solutions. This study underscores the necessity for further refinement of DMD like enhanced kinetic equations that account for local environmental factors and improved mean-field approximations better suited to complex interatomic potentials. Given the significant advantages DMD offers as a method, efforts in this direction are doubtlessly an interesting avenue for future research.

1. Introduction

Hydration in metal hydride nanostructures involves a complex interaction between hydrogen diffusion and lattice deformation. This interaction manifests itself in various phenomena, including phase transitions, swelling, and surface stress effects [4, 16, 21, 38, 39, 43]. These processes require a combined analysis of deformation and diffusion, while taking into account the discrete nature at the atomistic scale, where diffusion consists of infrequent events, such as hydrogen atoms oscillating within interstitial sites for extended periods before transitioning to an adjacent site [22].

Conventional molecular dynamics (MD) simulations integrate the equations of motion of atoms over time based on an interatomic potential describing their interactions [11]. This approach requires sufficiently small time steps to capture atomic vibrations and often necessitates a large number of time steps to observe a single infrequent event. This limitation hinders the use of MD for slow diffusive processes leading to a necessity for alternative methods like Kinetic Monte Carlo (MC) [41],

temperature-accelerated MD, hyperdynamics [22] and diffusive MD (DMD) [17]. This work focuses primarily on DMD.

DMD was first developed to simulate vacancy diffusion in metals over extended time scales [17, 27]. It approximates MD by representing atoms as sites that can be either occupied or vacant and tracking their occupation probabilities. Atom vibrations are modeled as Gaussian distributions around their expected positions, which are adjusted along with vibration frequencies to minimize free energy based on an interatomic potential, thereby allowing to consider deformation. Diffusion is approximated through an empirical kinetic equation that updates the occupation probabilities of neighboring sites based on current occupancy and free energy.

Since its introduction, DMD has undergone significant development, including extensions to solute diffusion [8, 9] and theoretical enhancements based on maximum entropy and relative entropy principles [30, 40]. DMD was further compared to correlated Gaussian phase packages and spin-diffusion [10, 13]. Applications span from studying vacancy diffusion in single-element metals and solute diffusion in binary alloys [8, 9, 12, 17, 27, 40], to modeling lithiation in silicon nanopillars [18] and hydration of palladium nanostructures [34–36].

Despite these advances, significant gaps remain in the validation and understanding of DMD. Current validation often focuses on properties in diffusion equilibrium, such as lattice and elastic constants or surface segregation [40]. Due to limited reference data, the verification of dynamic diffusive simulations is often limited to simplified cases like the diffusion of single atoms [17, 34] or cases with a fixed lattice [40, 42]. Additionally, used experimental reference data is suitable for determining the viability for specific use cases, yet provides limited insight into DMD-specific errors due to confounding factors such as interatomic potential choices and boundary conditions. Moreover, the accuracy and applicability of available kinetic equations lack a systematic comparison.

Diffusion in palladium-hydride nanostructures presents an ideal case to overcome those limitations of existing validations and further the understanding of DMD. Palladium-hydride is characterized by a low-hydrogen α-phase consisting of a face-centered cubic (FCC) palladium lattice with solute hydrogen atoms on octahedral interstitial sites, and a high-hydrogen β-phase with identical lattice structure but higher hydrogen concentration [1]. The diffusion-controlled transition between those phases is influenced by local lattice structures and stresses [1, 4] and accompanied by approximately 10% volume expansion, showing the strong deformation-diffusion coupling typical for DMD applications. The embedded atom model (EAM) potential developed by Zhou *et al* [45] has enabled detailed investigations using atomistic methods like MC [2, 6, 7, 25], MD [46, 47] and DMD [33–36, 40, 42]. Recent studies on palladium hydride also employed DMD to model slow diffusive processes and used the resulting configurations as starting point for MD simulations covering a shorter time scale [32]. This approach allows to gain deeper understanding of the involved processes and provides additional insight into the validity of the DMD solution. Existing DMD studies have however focused on slow phase transitions and phase boundary movement and the comparison with MD solutions was only conducted for the stability of the local equilibrium and not diffusive time scales. Yet, some diffusive processes occur within MD-accessible timescales [46], enabling a direct methodological comparison.

This study presents a comprehensive validation for DMD through a direct comparison with MD simulations of palladium-hydride for both static properties and diffusive processes. Comparative studies utilizing (accelerated) MD simulations have previously been employed to assess other time-bridging methods, such as the phase-field-crystal model [3, 24]. Using a similar approach utilizing identical EAM potentials and boundary conditions, these common external error sources are eliminated and the intrinsic error of DMD is isolated and quantified for various applications ranging from static bulk properties to complex diffusive processes. This framework addresses the aforementioned limitations of existing validation methods and offers new insights into DMD's accuracy and possible error sources. Additionally, the MD reference solution is leveraged to provide a novel comparison of four different kinetic equations commonly used for DMD across various diffusive phenomena in metal-hydrides. This enhances the understanding of their applicability and provides guidelines on their use while establishing a foundation and baseline for improvements.

The paper is organized as follows: section 2 summarizes the relevant DMD theoretical background. Section 3 compares DMD simulations of static properties with literature MD results, focusing on lattice and elastic constants. Section 4 extends this comparison to dynamic processes, presenting MD and DMD simulations using different kinetic equations for three cases: single atom bulk diffusion, surface segregation in a nanowire, and nanocube hydration. Section 5 summarizes the findings and provides conclusions and future research directions.

2. DMD

DMD is based on the separation of atomic motion into two distinct time scales: thermal oscillations of atoms around their mean positions within a local equilibrium, modeled by suitable probability distributions, and diffusive jumps changing this local equilibrium over time, modeled with kinetic equations. These two parts of the model are summarized in the following.

2.1. Local equilibrium state

2.1.1. Thermodynamic model

DMD represents the system through atom sites that can be vacant or occupied by a specific atom type. This representation enables modeling the behavior of the system in a local equilibrium, while allowing to update this state by changing the occupation of specific sites, which eliminates the requirement to explicitly track atom jumps. For vacancy diffusion, this is expressed through a binary occupation vector $\underline{\boldsymbol{n}}$, where each component n_i indicates whether atom site i is occupied or vacant. In the used model, each atom site is of a specific type and can only be occupied by this type.

Any microstate of the system is then defined by the occupation vector $\underline{\boldsymbol{n}}$ and the position and momentum matrices $\underline{\underline{\boldsymbol{q}}}$ and $\underline{\underline{\boldsymbol{p}}}$, where entries q_{ij} and p_{ij} represent the jth component of the position and momentum vector of atom site i, respectively [40]. DMD employs a microstates probability distribution $\rho\left(\underline{\underline{\boldsymbol{q}}},\underline{\underline{\boldsymbol{p}}},\underline{\boldsymbol{n}}\right)$ to eliminate the need for explicit tracking of thermal vibrations. This distribution is determined such that the expected value of quantities like energy or occupation match macroscopic values. This expected value $\langle A\rangle$ of an arbitrary quantity A is calculated by integrating its value weighted by the state probability over all possible microstates. For a system with N distinguishable particles, this takes the form

$$\langle A\rangle = \sum_{\underline{\boldsymbol{n}}\in\{0,1\}^N} \frac{1}{h^{3N}} \int_{\Gamma} A\left(\underline{\underline{\boldsymbol{q}}},\underline{\underline{\boldsymbol{p}}},\underline{\boldsymbol{n}}\right)\rho\left(\underline{\underline{\boldsymbol{q}}},\underline{\underline{\boldsymbol{p}}},\underline{\boldsymbol{n}}\right)\mathrm{d}q\mathrm{d}p, \tag{1}$$

where

$$\mathrm{d}q\mathrm{d}p = \prod_{i=1}^{N}\prod_{j=1}^{3}\mathrm{d}q_{ij}\mathrm{d}p_{ij} \tag{2}$$

and Γ represents the phase space of possible positions and momenta, $\sum_{\underline{\boldsymbol{n}}\in\{0,1\}^N}$ denotes the summation over all possible occupation vectors, and h is Planck's constant [40].

Assuming local equilibrium, where the average energy e_i of site i can be described as the expected value $\langle h_i\rangle = e_i$ of its Hamiltonian h_i, and its concentration x_i can be given as its average occupation $\langle n_i\rangle = x_i$, the probability distribution for such a vacancy problem is provided by [30]

$$\rho = \frac{1}{\mathcal{Z}}\prod_{i=1}^{N}|D|^{n_i-1}\exp\left(-\sum_{i}^{N}\beta_i h_i + \sum_{i}^{N}\beta_i\mu_i n_i\right) \tag{3}$$

with partition function

$$\mathcal{Z} = \sum_{\underline{\boldsymbol{n}}\in\{0,1\}^N}\frac{1}{h^{3N}}\prod_{i=1}^{N}|D|^{n_i-1}\int_{\Gamma}\exp\left(-\sum_{i}^{N}\beta_i h_i + \sum_{i}^{N}\beta_i\mu_i n_i\right)\mathrm{d}q\mathrm{d}p, \tag{4}$$

where β_i relates to the temperature of that atom site θ_i through $\theta_i = \frac{1}{k_B\beta_i}$ with Boltzmann constant k_B and μ_i represents the chemical potential. $|D|$ is the volume of possible atom site locations as introduced by Simpson *et al* to account for the indistinguishability of vacancy positions [30].

2.1.2. Mean-field approximation

The calculation of $\mathcal{Z}$ requires evaluating the phase integral, which is feasible only for simple cases. For general cases with a Hamiltonian

$$h_i\left(\underline{\underline{\boldsymbol{q}}},\underline{\boldsymbol{p}}_i\right) = \frac{n_i}{2m_i}\left|\underline{\boldsymbol{p}}_i\right|^2 + V_i\left(\underline{\underline{\boldsymbol{q}}}\right) \tag{5}$$

consisting out of kinetic energy (dependent on the mass m_i and momentum $\underline{\boldsymbol{p}}_i$ of the atom site) and a more complex interatomic potential V_i like the used EAM potential, this is not feasible.

To address this limitation, the probability distribution is approximated by replacing h_i in equations (3) and (4) with a set of simplified trial Hamiltonians h_{i0}. This yields a trial probability distribution

$$\rho_0 = \frac{1}{\mathcal{Z}_0} \prod_{i=1}^{N} |D|^{n_i - 1} \exp\left(-\sum_i^N \beta_i h_{i0} + \sum_i^N \beta_i \mu_i n_i \right) \tag{6}$$

with corresponding trial partition function

$$\mathcal{Z}_0 = \sum_{\underline{\boldsymbol{n}} \in \{0,1\}^N} \frac{1}{h^{3N}} \prod_{i=1}^{N} |D|^{n_i - 1} \int_\Gamma \exp\left(-\sum_i^N \beta_i h_{i0} + \sum_i^N \beta_i \mu_i n_i \right) \mathrm{d}q\mathrm{d}p, \tag{7}$$

which becomes computationally feasible given a suitable set of trial Hamiltonians. The trial Hamiltonians h_{i0} generally depend on a set of mean-field parameters. Through the application of relative entropy principles [30], those parameters can be optimized to achieve the closest possible approximation to ρ. This optimization can be formulated as a minimization problem for the DMD free energy $\mathcal{F}$ within the subspace of the used trial Hamiltonians. This provides an upper bound to the true free energy F as

$$F \leqq \mathcal{F} = \sum_i^N \left(\langle h_i - h_{i0} \rangle_0 + \mu_i x_i \right) - \beta_i^{-1} \log \mathcal{Z}_0, \tag{8}$$

where the notation $\langle \rangle_0$ denotes the macroscopic average as defined in equation (1), but evaluated using the trial probability distribution ρ_0 rather than ρ.

2.1.3. Choice of trial Hamiltonian

The approach of Venturini *et al* [40] is adopted for the kinetic energy of the trial Hamiltonians under the additional assumption of zero average momentum due to the quasi-static nature of the present use case. The approach of Simpson *et al* is followed for the potential energy, which is modeled as a harmonic potential with frequency ω_i around the mean position $\bar{\underline{\boldsymbol{q}}}_i$ of the atom site, while ensuring that the energy of vacancies is zero [30]. The resulting trial Hamiltonian

$$h_{i0}\left(\underline{\boldsymbol{q}}_i, \underline{\boldsymbol{p}}_i, n_i \right) = \frac{n_i}{2m_i} \left| \underline{\boldsymbol{p}}_i \right|^2 + \frac{n_i m_i {\omega_i}^2}{2} \left| \underline{\boldsymbol{q}}_i - \bar{\underline{\boldsymbol{q}}}_i \right|^2 \tag{9}$$

has the same kinetic energy as equation (5), but the approximation of the potential energy depends only on the position $\underline{\boldsymbol{q}}_i$ of the site and does not contain explicit interactions between sites, which simplifies the evaluation of the phase integral. Substituting this trial Hamiltonian into equation (7) yields the trial partition function

$$\mathcal{Z}_0 = \prod_{i=1}^{N} \left[1 + \frac{\mathrm{e}^{\beta_i \mu_i}}{\left(\hbar \beta_i \omega_i \right)^3} \right], \tag{10}$$

where $\hbar = \frac{h}{2\pi}$ represents the reduced Planck constant. Evaluating the averages in equation (8) with this set of trial Hamiltonians yields

$$\mathcal{F} = \frac{1}{\beta_i} \sum_i^N \left[\beta_i \langle V_i \rangle_0 - \frac{3}{2} x_i + 3 x_i \log\left(\hbar \beta_i \omega_i \right) + (1 - x_i) \log\left(1 - x_i \right) + x_i \log x_i \right] \tag{11}$$

as the DMD free energy. This functional parallels that derived in [19], differing only by a factor x_i preceding the logarithm term. This difference originates from the factor n_i in the harmonic potential of the trial Hamiltonian and ensures vacancies do not contribute energy, making this formulation particularly suitable for vacancy problems. Minimizing $\mathcal{F}$ with respect to the mean-field parameters optimally approximates the local equilibrium behavior in the subspace of the trail Hamiltonians and yields each site's frequency ω_i and mean position $\bar{\underline{\boldsymbol{q}}}_i$ for given concentrations x_i.

2.2. Kinetic equations

The local equilibrium established by minimizing equation (11) is developed over time by updating the expected occupation x_i of each site i through kinetic equations. Assuming changes in x_i result from exchanges with the set of its nearest neighbors N_i, the time derivative $\dot{x}_i$ of the concentration takes the form $\dot{x}_i = \sum_{j \in N_i} J_{ij}$, where J_{ij} represents the concentration exchange function between site i and j and $\mu_i = \frac{\partial \mathcal{F}}{\partial x_i}$ denotes the chemical potential at site i [17]. J_{ij} is chosen empirically with $J_{ij} = -J_{ji}$ to ensure mass conservation. Common choices for J_{ij} are summarized in the following and analyzed in this study. An isotherm state with constant β at all atom sites is assumed as not all kinetic equations are available in the literature as a function of β_i.

2.2.1. Linear kinetics

The simplest kinetic equations follow a linear relationship with the chemical potential difference of the form

$$\frac{\partial x_i}{\partial t} = k_\mathrm{B}\beta \sum_{j \in N_i} B_{ij} \frac{x_i + x_j}{2} \left(\mu_j - \mu_i\right), \tag{12}$$

where B_{ij} represents an exchange coefficient between sites i and j [40]. While B_{ij} allows for a dependency on the local environment, this is commonly neglected by assuming a constant global exchange coefficient B_0. This simplifies the linear kinetic equation to

$$\frac{\partial x_i}{\partial t} = B_0 k_\mathrm{B}\beta \sum_{j \in N_i} \frac{x_i + x_j}{2} \left(\mu_j - \mu_i\right), \tag{13}$$

which will be referred to as DMD-Linear.

2.2.2. Master equation

More sophisticated approaches incorporate the underlying atomic jump processes, which can only occur between occupied and vacant sites. The probability of a successful jump depends on the driving force, i.e. the difference in chemical potential, and an energy barrier. This leads to the phenomenological master equation

$$\frac{\partial x_i}{\partial t} = \sum_{j \in N_i} \nu \mathrm{e}^{-\beta Q_{bij}} \left[x_j \left(1 - x_i\right) \mathrm{e}^{c\beta\left(\mu_j - \mu_i\right)} - x_i \left(1 - x_j\right) \mathrm{e}^{c\beta\left(\mu_i - \mu_j\right)} \right], \tag{14}$$

where ν denotes the attempt frequency and Q_{bij} represents the barrier energy between sites i and j [17, 18, 23]. The parameter c takes values of either 1.0 [18] or 0.5 [19, 23] in the DMD literature. Similar to B_{ij}, the barrier energy is commonly chosen as a global constant Q_b independent of the local environment of the atom sites, which simplifies the master equation to

$$\frac{\partial x_i}{\partial t} = \nu \mathrm{e}^{-\beta Q_b} \sum_{j \in N_i} \left[x_j \left(1 - x_i\right) \mathrm{e}^{c\beta\left(\mu_j - \mu_i\right)} - x_i \left(1 - x_j\right) \mathrm{e}^{c\beta\left(\mu_i - \mu_j\right)} \right]. \tag{15}$$

The master equation with $c = 0.5$ and 1.0 are denoted in the following as DMD-M-0.5 and DMD-M-1.0, respectively.

For vacancy diffusion, the master equation can also be based on the vacancy formation energy f_i as

$$\frac{\partial x_i}{\partial t} = \nu \mathrm{e}^{-\beta Q_b} \sum_{j \in N_i} \left[x_j \left(1 - x_i\right) \mathrm{e}^{\frac{\beta}{2}\left(f_j - f_i\right)} - x_i \left(1 - x_j\right) \mathrm{e}^{\frac{\beta}{2}\left(f_i - f_j\right)} \right], \tag{16}$$

where $f_i = \mu_i - \log \frac{x_i}{1 - x_i}$ is calculated as chemical potential minus the configurational entropy contribution $\log \frac{x_i}{1 - x_i}$ [17]. This approach is referred to as DMD-M-Vac.

2.2.3. Calibration

The kinetic equations in equations (13), (15) and (16) each contain a global scalar factor which is used to calibrate the simulated diffusive time to the physical time. This calibration can be achieved through direct experimental observations [34–36] or via the macroscopic diffusion constant D_H using the long-wavelength limit [17, 40]. Following the latter approach results in

$$B_0 = \frac{D_\mathrm{H}}{k_\mathrm{B} a_0^2} \tag{17}$$

for the linear equation, with a_0 as the lattice constant [40]. Similar principles yield

$$\nu \mathrm{e}^{-\beta Q_b} = \frac{D_\mathrm{H}}{(2c+1)\, a_0^2} \tag{18}$$

for equation (15) and

$$\nu \mathrm{e}^{-\beta Q_b} = \frac{D_\mathrm{H}}{a_0^2} \tag{19}$$

for (16), details of which are given in appendix. Recent DMD implementations not considered in this work enable to determine attempt frequency and energy barriers on-the-fly [20].

2.3. Implementation

The used implementation is built on the MXE user-package for LAMMPS [37] published by Mendez and Ponga [19]. This user-package is extended by the presented trial Hamiltonians and the different kinetic equations. Key details of this implementation are summarized in the following.

2.3.1. DMD algorithm

The implementation of [19] follows a staggered scheme, alternating between concentration evolution via forward Euler integration of kinetic equations and dynamic relaxation optimization of frequencies and mean positions. While the original implementation [19] includes adaptive time-step controls to prevent concentrations from exceeding physical maximum and minimum values, this approach proved restrictive for DMD-Linear, frequently resulting in extremely small time steps near these boundaries. To address this limitation, a subcycling scheme similar to [34] was used for DMD-Linear, iterating the diffusive step until reaching either a minimum concentration change threshold at any atom site or a maximum iteration count before system relaxation. Furthermore, for DMD-Linear, minimal boundary value violations were permitted to maintain computational efficiency without compromising accuracy. All such simulations where repeated with different thresholds for the subcycling scheme and permitted limit violations to ensure convergence to the correct solution.

2.3.2. Numerical integral of the phase integral

Minimizing equation (11) requires evaluating $\langle V_i \rangle_0$ through numerical integration. In the used implementation, a third-order Gauss–Hermite quadrature rule with two quadrature points per phase integral dimension is employed [19]. While this approach efficiently handles pair potentials with twelve quadrature points, the EAM potential's embedding function, dependent on multiple neighbor positions, requires a high number of quadrature points. This limitation is solved by linearizing the embedding function around its value at the mean position of the atoms sites, enabling integration with the same quadrature points as pair functions [19]. This integration method is used unless stated otherwise.

Additionally, a MC-based numerical integration method was implemented for the static properties in section 3 to quantify potential quadrature errors. For this method, 125 pairs of three-dimensional points $\underline{\boldsymbol{MC}}_1$ and $\underline{\boldsymbol{MC}}_2$ were sampled from a standard normal distribution at the beginning of the simulation. To preserve symmetry, these points were combined into the sets $(\underline{\boldsymbol{MC}}_1, \underline{\boldsymbol{MC}}_2)$, $(-\underline{\boldsymbol{MC}}_1, -\underline{\boldsymbol{MC}}_2)$, $(\underline{\boldsymbol{MC}}_2, \underline{\boldsymbol{MC}}_1)$ and $(-\underline{\boldsymbol{MC}}_2, -\underline{\boldsymbol{MC}}_1)$. The resulting 500 six-dimensional MC quadrature points were then used to integrate the pair functions following the methodology described in [19].

3. Numerical results for static properties

Zhou *et al* [47] conducted MD simulations using an EAM potential [45] to evaluate PdH lattice and elastic constants across various temperatures and homogeneous hydrogen concentrations. These simulations serve as reference for the DMD validation. Their study employed an $8 \times 8 \times 8$ supercell of FCC palladium with $\langle 100 \rangle$, $\langle 010 \rangle$ and $\langle 001 \rangle$ axes aligned with coordinate axes, a fitting number of hydrogen atoms on octahedral interstitial sites and periodic boundary conditions [47]. Using an NPT ensemble (constant number of atoms, pressure and temperature) at zero stress, lattice constants were determined from time-averaged simulation box dimensions. Elastic constants were calculated by deforming new samples based on those lattice constants in an NVT ensemble (constant number of atoms, volume and temperature) and measuring time-averaged stress responses.

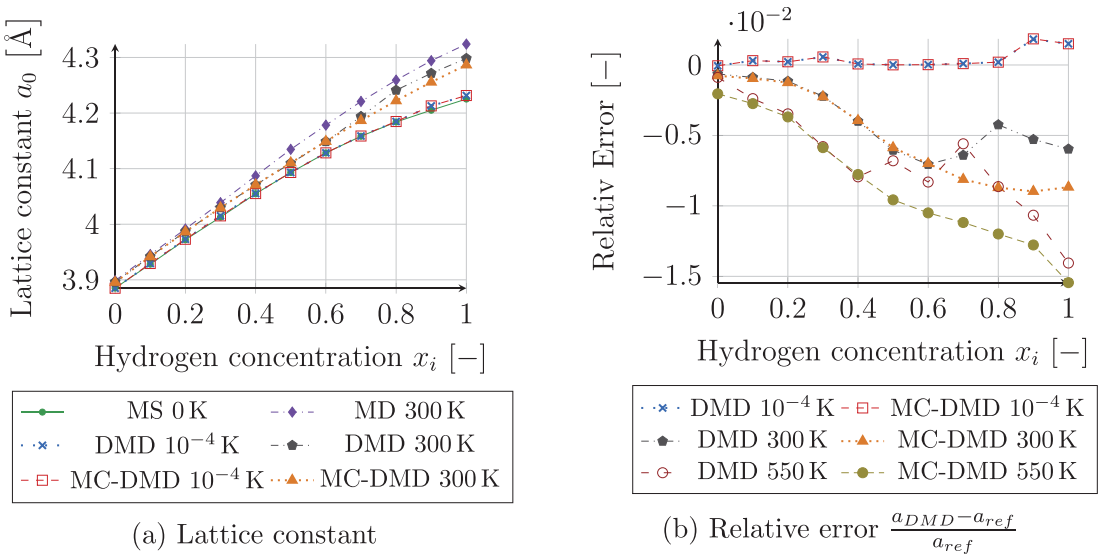

(a) Lattice constant (b) Relative error $\frac{a_{DMD}-a_{ref}}{a_{ref}}$

Figure 1. (a) MS/MD, DMD and MC-DMD calculated lattice constants a_0 and (b) relative DMD error as functions of hydrogen concentration at different temperatures. MS/MD data from [47].

3.1. DMD simulation set-up

A constant homogeneous hydrogen concentration was assumed for the DMD analysis as the small MD sample size prohibits phase separation. Under these conditions, DMD sites of identical species in a perfect lattice exhibit uniform behavior, enabling the use of small periodic samples. A $2 \times 2 \times 2$ supercell of FCC palladium with the same orientation as the reference study and hydrogen sites on all octahedral interstitial sites were employed. All initial configurations in this work were generated with Atomsk [14]. The concentration of all palladium sites was set to unity and samples with homogeneous hydrogen concentrations ranging from 0.0 to 1.0 at 0.1 intervals are analyzed at 0.0001 K, 300 K and 550 K. The same EAM potential as for the reference study was employed.

Each sample was relaxed by minimizing equation (11) with respect to frequency and mean positions using dynamical relaxation while adjusting the box dimensions automatically based on the present stress in a manner similar to the NVT ensemble of the MD simulations to ensure zero stress. The relaxed volume was used to determine a_0. Following the approach of [47], new samples were created based on this lattice constant to compute the elastic constants. The stiffness tensor is expressed in Voigt notation, where the second-order stress and strain tensors are represented as six-component vectors $\underline{\boldsymbol{\sigma}}$ and $\underline{\boldsymbol{\varepsilon}}$. A small strain $\varepsilon_k = \pm 10^{-4}$ was applied to the k-th strain component while keeping all other components zero. The tensile (C_{11}) and shear (C_{44}) elastic constants were computed from the virial stress response as $C_k = \frac{\partial \sigma_k}{\partial \varepsilon_k} \approx \frac{\Delta \sigma_k}{\Delta \varepsilon_k}$. The bulk modulus B was determined through hydrostatic strain ($\varepsilon_1 = \varepsilon_2 = \varepsilon_3 = 10^{-4}$) with $B = -V\frac{\Delta p}{\Delta V}$, where V represents the sample volume, and Δp and ΔV denote pressure and volume changes. This uniquely determines the elastic behavior as only three elastic constants are independent due to the crystal symmetry. All simulations were conducted using both the standard third-order Gauss–Hermite quadrature (hereafter referred as DMD) and the MC-based quadrature described in section 2.3.2 (referred to as MC-DMD).

3.2. Results

Figure 1(a) compares DMD-calculated lattice constants at 0.0001 K and 300 K with molecular static (MS) reference solutions at 0 K and MD reference solutions at 300 K taken from [47]. Both approaches demonstrate increasing lattice constants with rising hydrogen concentration. DMD results at 0.0001 K closely match the MS reference independent of integration method, while results at 300 K show increasing deviation from MD references at higher hydrogen concentrations, which is more pronounced for MC integration of the phase integral. Figure 1(b) illustrates the relative DMD error $\frac{a_{\mathrm{DMD}}-a_{\mathrm{ref}}}{a_{\mathrm{ref}}}$ compared to the respective reference solutions a_{ref}, revealing error growth with both temperature and hydrogen concentration.

Figure 2 presents DMD-calculated elastic constants as function of hydrogen concentration at 0.0001 K and 300 K, alongside MS and MD reference solutions from [47]. Independent of integration method, the DMD results at 0.0001 K track the MS results at 0 K closely and show small deviations at higher hydrogen concentrations. At 300 K, the MD and DMD results are comparable at low hydrogen concentration

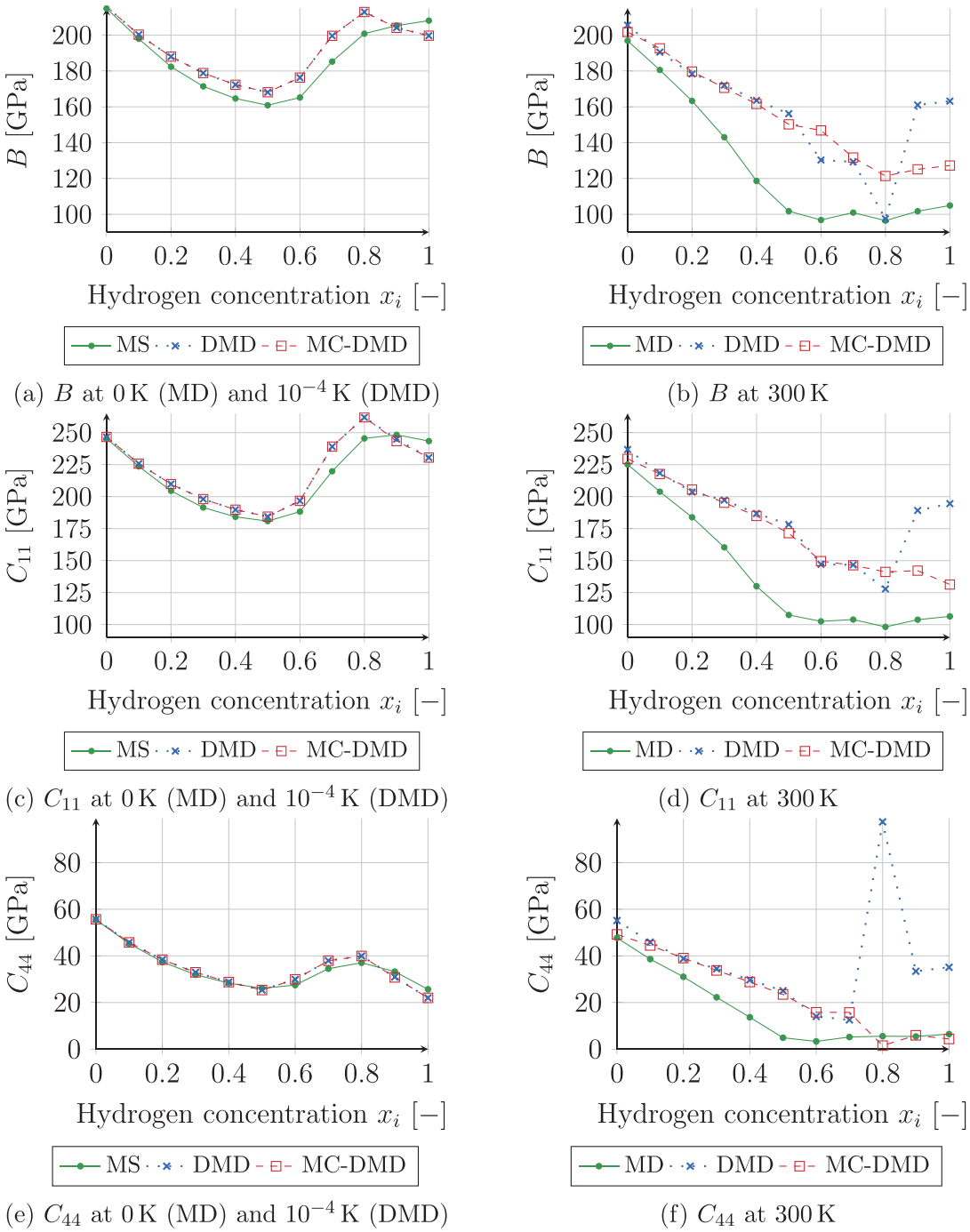

Figure 2. MS/MD, DMD and MC-DMD calculated elastic constants as function of hydrogen concentration at different temperatures. MS/MD data from [47] with $C_{11} = B + \frac{4}{3}C'$.

but show significant discrepancies at higher hydrogen concentrations. Using the classic Gauss–Hermite quadrature rule additionally introduces jumps and outlier data points absent in MD data and MC-DMD.

3.3. Discussion

This section discusses the errors introduced by the primary approximations in DMD for static cases without use of kinetic equations: (i) atomic self-interaction resulting from representing atoms as sites with average concentrations (x_i) rather than binary occupations (n_i), (ii) the numerical integration of interatomic potentials in equation (11) and (iii) the omission of correlated vibrations within the local harmonic mean-field approximation. Additionally, the computational speed-up factor and comparisons with existing experimental data are discussed.

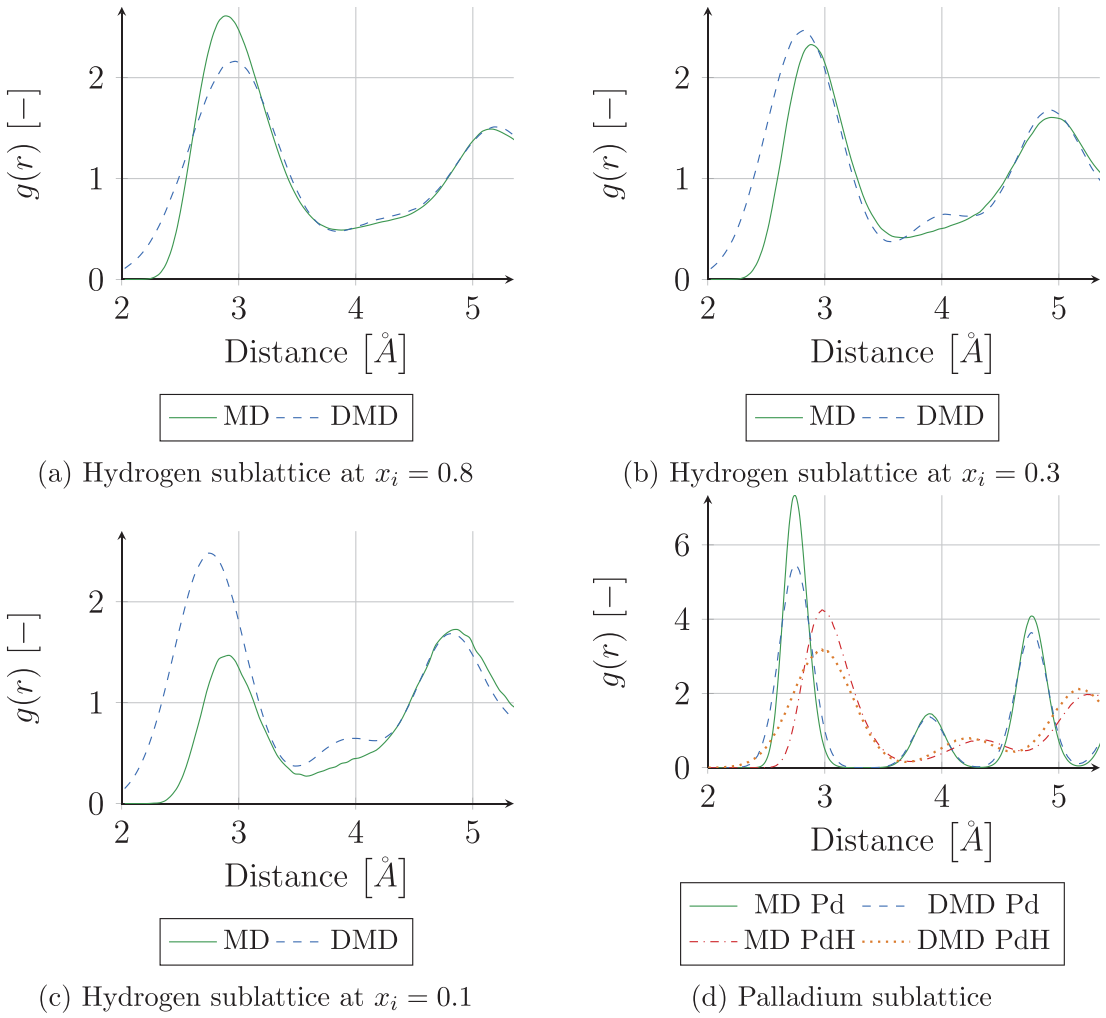

(a) Hydrogen sublattice at $x_i = 0.8$

(b) Hydrogen sublattice at $x_i = 0.3$

(c) Hydrogen sublattice at $x_i = 0.1$

(d) Palladium sublattice

Figure 3. (a)–(c) Radial distribution function $g(r)$ of the hydrogen sublattice at different hydrogen concentrations x_i at 300 K (d) radial distribution function $g(r)$ of the palladium sublattice for pure palladium and fully saturated palladium hydride at 300 K.

3.3.1. Self-interaction

By representing atoms as sites with average concentrations (x_i) rather than binary occupations (n_i), DMD treats site occupations as independent variables. In physical systems, these occupations are inherently correlated because a single atom cannot occupy multiple sites simultaneously. Neglecting this correlation leads to 'self-interaction' errors between partially occupied sites and an overestimation of the phase average $\langle n_i n_j \rangle$ for sites of the same species. These errors are limited to hydrogen-hydrogen interactions in this study, as all palladium sites remain fully occupied.

Several lines of evidence suggest that while self-interaction is present, it is not the primary driver of the observed discrepancies between MD and DMD. First, self-interaction is a combinatorial error of the occupation treatment and no strong temperature-dependency is expected, which is in contrast to the temperature behavior observed for the error of lattice and elastic constants. Second, self-interaction errors should vanish as hydrogen concentration approaches $x = 1$ (full occupancy), yet errors in lattice and elastic constants persist in this limit.

Radial distribution functions (RDFs) of the hydrogen sublattice at 300 K, based on MD simulations replicating [47], further support this conclusion (figures 3(a)–(c)). At high concentrations (figure 3(a)), the DMD and MD distributions match closely. Minor differences near the nearest-neighbor peak diminish when integrating over the radius, suggesting they merely represent a different distribution of distances. As the hydrogen concentration decreases (figures 3(b) and (c)), the MD RDF correctly omits the reference atom from the local density, resulting in lower peak intensities. The DMD distributions do not exhibit this reduction because the method fails to distinguish between an atom's self-contribution and

the surrounding hydrogen environment. This confirms that self-interaction is prominent at low concentrations. However, since DMD is the most reliable in this regime, it suggests that self-interaction is a secondary effect, likely overshadowed by dominant Pd–Pd and Pd–H interactions which remain unaffected by this error.

3.3.2. Numerical integration

The distance of quadrature points from the mean positions during the numerical integration of $\langle V_i \rangle_0$ in equation (11) scales with $\sqrt{\theta_i}$. Consequently, the choice of integration method becomes negligible near 0 K, as confirmed by figures 1 and 2. These figures also demonstrate that while the Gauss–Hermite quadrature rule is sufficient for low hydrogen concentrations at 300 K, the integration error relative to MC-DMD increases as hydrogen content grows.

This discrepancy is driven by the EAM potential's palladium-palladium pair function, which exhibits an overshooting non-monotonic decay to zero close to the cutoff distance. This overshoot results in a small region with rapidly changing and at the cut-off discontinuous derivative, where a high number of quadrature points is required for accurate numerical integration. The influence of this region can be deducted from the RDFs of palladium atoms for MD and DMD simulations depicted in figure 3(d). The upper limit of the radial distance axis of this graphic coincides with the cutoff distance and so shows the palladium density at this distance. This density is low for pure palladium as the cutoff is between two neighbor distances, indicating a low influence. Increasing hydrogen content shifts neighbor distances until at concentration of 1.0 the third-nearest neighbor peak approaches the cutoff distance, amplifying its influence, which coincides with the growing discrepancies between Gauss–Hermite and MC quadrature DMD results in figures 1 and 2.

This problem is amplified by crystal symmetry making many quadrature points equivalent and further reducing the number of unique evaluation points. For Gauss–Hermite quadrature, the number of quadrature points in this sensitive region highly influences the mechanical behavior and points entering and leaving this region cause the discontinuities observed in figure 2. Using MC integration avoids this problem by correctly integrating this region with a sufficient number of unique evaluation points and so provides an improved match for the elastic constants void of discontinuities. This comparison highlights the influence of integration method for this use case and advocates for more advanced integration method, such as a recently developed machine learning based quadrature to balance accuracy with computational efficiency [28]. Not depicted tests with higher order Gauss–Hermite quadrature rules on the other hand did not show any improvement as they suffer from the same lack of unique evaluation points caused by crystal symmetry. This behavior is expected less severe for non-periodic samples as the distorted crystal symmetry leads to more unique quadrature points. For this reason and due to the high computational cost of MC integration, only Gauss–Hermite quadrature has been used in all following examples.

3.3.3. Correlated vibrations

Figure 3 shows that while DMD RDFs align well with MD results for distances beyond the nearest-neighbor peak, significant discrepancies in nearest-neighbor peak height and width persist. These differences are evident even in cases with minimal/no self-interaction (figures 3(a) and (d)). This behavior stems from correlation in vibrations between neighboring atoms. While MD captures these correlations, the DMD trial Hamiltonian in equation (9) using a local harmonic approximation models vibrations as independent Gaussian distributions. The neglect of these correlations results in broader, lower peaks in DMD compared to MD. As shown by the evolution of the average Pearson correlation coefficient in figure 4, this positional correlation between palladium atoms grows with hydrogen content, leading to a corresponding increase in the approximation error, indicating a measurable influence of the approximation.

3.3.4. Computational speed-up

A comprehensive analysis of the computational speed-up achieved by DMD is beyond the scope of this work, as the used DMD implementation prioritized numerical stability and ease of use over maximum efficiency. For example, a $2 \times 2 \times 2$ supercell was employed instead of a single cell to better detect potential inhomogeneous frequency patterns and a stable, albeit less efficient, minimization method was utilized. Furthermore, because the MD results in this section were sourced from literature, direct comparisons of the underlying computational effort are limited. Nevertheless, estimates based on the MD steps reported in [47] and the performance observed in this work suggest that DMD is approximately two orders of magnitude faster than the MD setup in [47] for lattice constant calculations. For elastic

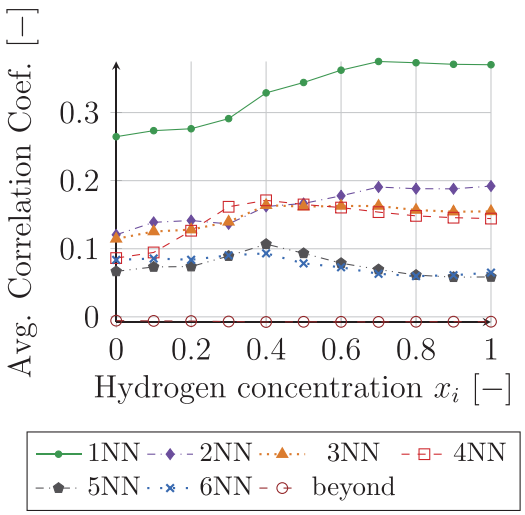

Figure 4. Pearson correlation coefficient of displacements of palladium atoms between successive output frames during MD simulations at 300 K as function of hydrogen concentration. Correlation is categorized and averaged by neighbor shell from nearest neighbor (1NN) to sixth nearest neighbor (6NN).

constants, the speed-up reaches four orders of magnitude, primarily due to the larger sample sizes and extensive time-averaging required by MD to achieve reliable results.

3.3.5. Comparison with experimental data

Because this work benchmarks DMD directly against MD using the same interatomic potential, experimental data does not provide additional insights into the intrinsic accuracy of the DMD approximations. However, comparing results to experimental values remains valuable to demonstrate the necessity of such direct benchmarking studies, as it helps distinguish errors inherent to the thermodynamic method from those stemming from the underlying interatomic potential. MD and DMD results demonstrate good agreement with experimental observations at low temperatures independent of concentration and at room temperature with low hydrogen concentration (see [47] for a comparison between MD-calculated lattice and elastic constants and experimental values from the literature). Yet, both approaches show notable discrepancies at higher concentrations. Experimental values for palladium hydride at $x = 0.607$ and $T = 298\,\mathrm{K}$ show a lattice constant of 4.025 Å [1], which is notably smaller than both MD and DMD results. Experimentally determined elastic constants B and C_{44} at $T = 300\,\mathrm{K}$ and $x = 0.66$ are with 190.0 GPa and 71.3 GPa, respectively, significantly stiffer than the numerical values [15]. Further experimental data corroborates this discrepancy [26, 29].

The DMD predictions of lattice and elastic constants under those conditions exhibit a similar trend as MD results, yet are in better agreement with experimental measurements than the MD counterparts. This method-independent discrepancy with experimental observations confirms a predominant influence of the EAM potential, wherein the smaller DMD error partially offsets the EAM-inherent error. This observation corroborates the requirement of evaluating DMD against MD reference solutions utilizing the same EAM potential instead of experimental data to isolate and quantify DMD's inherent approximation errors independent of potential-related uncertainties. For this reason, a detailed comparison with experimental data is beyond the scope and focus of this work and the comparison is limited between MD and DMD results. For a more detailed comparison of MD-calculated lattice and elastic constants with experimental measurements in the literature and possible causes it is referred to [47].

4. Numerical results for diffusive processes

4.1. Single atom bulk diffusion

The simplest case of hydrogen diffusion in palladium consists out of a single hydrogen atom in an infinite perfect palladium lattice. Due to crystal symmetry, all neighboring interstitial sites are equivalent. Jumps to neighboring sites are therefore of equal probability and the hydrogen atom approximately behaves as a random walker on a three-dimensional lattice. While previous studies have validated DMD

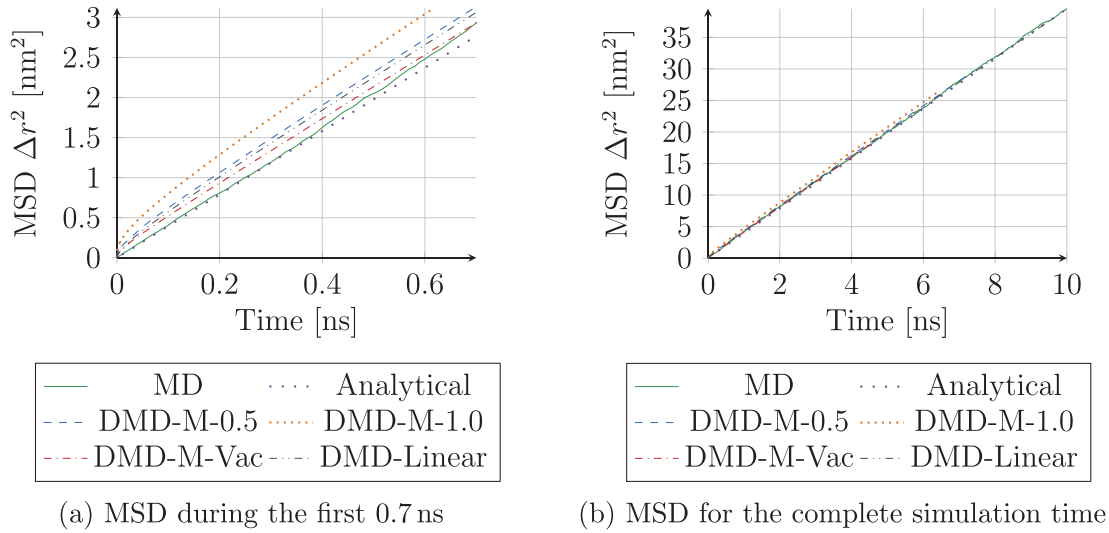

(a) MSD during the first 0.7 ns (b) MSD for the complete simulation time

Figure 5. Analytical MSD (equation (20)) and MD/DMD calculated MSD of a single hydrogen atom as function of time.

against the analytical solution of a random walker for both vacancy diffusion in copper [17] and hydrogen diffusion in palladium [34], a systematic comparison between different DMD kinetic equations, MD simulations and this analytical solution remains unexplored.

4.1.1. MD simulations

The MD simulations employed a $5 \times 5 \times 5$ FCC palladium supercell containing a single hydrogen atom positioned at an octahedral interstitial site and used periodic boundary conditions. Simulations were performed in an NPT ensemble with zero average pressure at 300 K for 10.2 ns with a 1.0 fs time step. The first 0.2 ns were excluded from analysis to avoid initial non-equilibrium effects and the configuration after 0.2 ns was considered as the reference state. The mean squared displacement (MSD) Δr^2 of the hydrogen atom was calculated relative to this reference position. Statistical significance was achieved by averaging results of 2000 independent simulations with different randomized initial velocities. The resulting average MSD is shown in figure 5.

Additionally, the temporal evolution of the average concentration at the initially occupied octahedral site was tracked by determining the fraction of simulations where the hydrogen atom is within half the nearest neighbor distance of its reference position. To increase statistical significance at low concentrations, the number of independent simulations was increased to 20 000. Segments of 2 ns were extracted from those trajectories in 0.4 ns intervals, assuming statistical independence between segments. This approach yields 420 000 such segments as samples for analyzing the concentration evolution at the initially occupied site, which is presented in figure 6.

4.1.2. Random walker analytical solution

The analytical MSD for a random walker in a 3D FCC lattice with isotropic diffusion follows

$$\Delta r^2 = 6 D_\mathrm{H} t, \tag{20}$$

where D_H represents the hydrogen diffusion constant in palladium and t denotes the time [5]. This relationship was used to determined D_H from the MD-derived MSD to $D_\mathrm{H} \approx 65.9\,\text{Å}^2\,\text{ns}^{-1}$. The resulting analytical MSD evolution depicted in figure 5 closely matches the MD results, with minor deviations attributable to finite sampling effects. The concentration at distance $\tilde{r}$ from the initially occupied site follows [5]

$$x(r,t) = \frac{a_0^3}{32\,(\pi D_\mathrm{H} t)^{\frac{3}{2}}} \exp\left(-\frac{\tilde{r}^2}{4 D_\mathrm{H} t}\right), \tag{21}$$

which evaluated at zero distance provides the analytical solution for the expected concentration of the initially occupied site shown in figure 6.

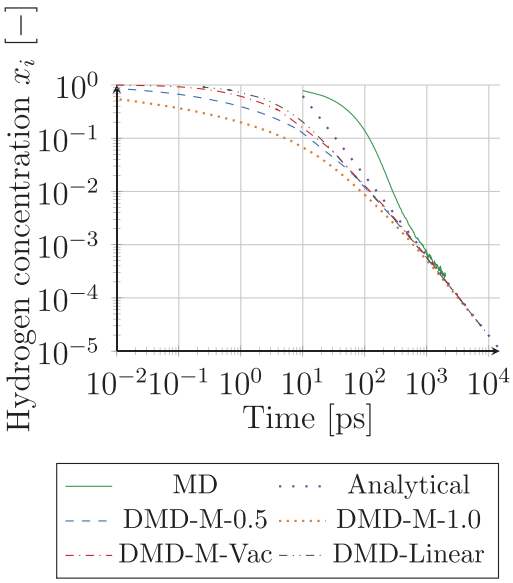

Figure 6. Hydrogen concentration at the initially occupied octahedral site as function of time for the different used simulation methods compared to the analytical solution of equation (21).

4.1.3. DMD simulations

DMD simulations utilized a $75 \times 75 \times 75$ FCC palladium supercell with hydrogen sites at all octahedral interstitial positions under periodic boundary conditions. A minimum concentration threshold of $x_{\min} = 1.0 \cdot 10^{-6}$ was implemented across all sites to ensure numerical stability. The central hydrogen site was initialized with $x_i = 1.0$ and all other sites with $x_{\min}$. The DMD simulations employed the kinetic equations detailed in section 2.2, which were calibrated according to section 2.2.3 to match the MD-derived diffusion constant. The time step was chosen adaptively with step-wise increased maximum time step as the chemical potential gradient decreases over time. Simulations were stopped once periodic images started interacting.

The resulting MSD evolution, calculated from concentration and distance of all hydrogen sites, is presented in figure 5. In contrast to both analytical and MD results, the DMD simulations exhibit non-linear MSD behavior during the initial 0.2 ns, with an elevated initial slope. Long-time behavior converges to the expected results, with the kinetic equations DMD-M-Vac and DMD-Linear showing the most rapid convergence, while DMD-M-1.0 and DMD-M-0.5 demonstrate larger early-time deviations.

The concentration evolution at the initially occupied site (figure 6) reveals similar trends. All DMD implementations initially deviate from the analytical solution but achieve good agreement after sufficient time, with DMD-M-Vac and DMD-Linear again showing superior convergence towards the expected solution compared to DMD-M-1.0 and DMD-M-0.5.

4.1.4. General discussion

The MD-derived hydrogen diffusion constant matches the values stated in [46], validating the MD simulations. The DMD results successfully reproduce both MSD and local concentration behavior at long times, regardless of the chosen kinetic equation. This convergence stems from the reduced concentration gradients after sufficient time has passed. Under those conditions all kinetic equations effectively reduce to linear behavior around their calibration point. This validates the implementation for typical slow diffusive processes characterized by modest chemical potential gradients.

Early-time behavior shows systematic deviations from reference solutions for several reasons: First, the analytical solution is only valid after sufficient time for a large number of jumps has passed, as evident by the mismatch with MD results. Second, the kinetic equations were calibrated for small chemical potential differences, while the initial state features sharp gradients. Lastly, DMD restricts transitions to nearest neighbors, whereas for MD simulations chain jumps over several neighbor distances are observed. Those chain jumps are also not considered for the analytical solution, explaining the mismatch with the MD results.

Among the implemented kinetic equations, DMD-M-Vac and DMD-Linear demonstrate superior behavior in all measured quantities while DMD-M-1.0 and DMD-M-0.5 require longer until they match the reference solution.

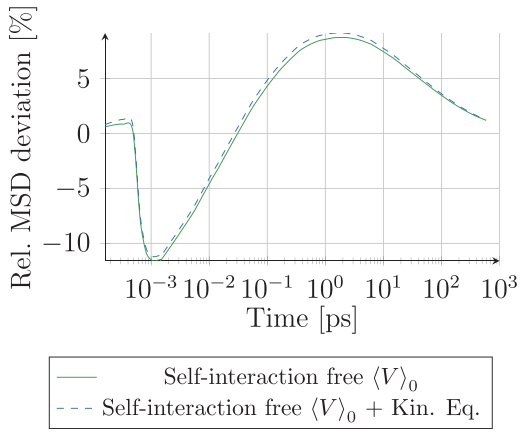

Figure 7. Influence of self-interaction in $\langle V \rangle_0$ and equation (15) on the MSD of DMD-M-1.0. The unmodified DMD-M-1.0 simulation serves as the baseline for the relative difference.

While the rapid diffusion of hydrogen in palladium enables direct benchmarking between MD and DMD, this high mobility also complicates the calculation of representative speed-up factors. The possible time step in DMD is governed by the fastest diffusive processes. Consequently, the time steps in this specific study are uncharacteristically small. Practical applications of DMD beyond the time-scales accessible to MD typically allow for time steps several orders of magnitude larger. For a more general comparison of the time scales accessible to both methods, the reader is referred to [20, 32].

4.1.5. Self-interaction

The case of a single diffusing hydrogen atom offers a unique opportunity to isolate the influence of spurious self-interactions in both the potential energy $\langle V_i \rangle_0$ and the kinetic equations, since any hydrogen-hydrogen interaction is necessarily an artifact of DMD. To quantify the impact of these interactions during the integration of the potential, the DMD-M-1.0 simulations were repeated for the most relevant first 0.6 ns with hydrogen-hydrogen interactions explicitly disabled. As shown in figure 7, the deviation in MSD between this modified approach and the standard DMD-M-1.0 simulations is minimal during the initial steps since the hydrogen concentration is localized at the central site, rendering self-interaction effects negligible. The discrepancy increases as the concentration spreads to neighboring sites while remaining sufficiently clustered to allow for erroneous self-interactions. Once the hydrogen concentration disperses over a wider area, the influence of these interactions diminishes and the results converge toward the standard DMD-M-1.0 behavior.

While the impact of self-interaction is notable here, this setup represents an extreme case scenario for this system as all hydrogen-hydrogen interactions are non-physical self-interactions and the hydrogen concentration initially is restricted to a few adjacent sites. This demonstrates that even under such unfavorable conditions, self-interaction is not the dominant error source and is, for instance, overshadowed by the choice of kinetic equation.

In addition to spurious interaction between hydrogen atoms in $\langle V_i \rangle_0$, the master equation also is susceptible to self-interaction effects. Terms like $x_j(1-x_i)$ take into account that a jump can only occur from an occupied to an empty site. Yet, since a single atom cannot occupy both sites concurrently, the two probabilities are dependent, which is not considered for the standard kinetic equation. This becomes particularly evident in this single-hydrogen case, where the occupancy of site j implies all other sites are empty. Under these conditions, equation (15) simplifies to

$$\frac{\partial x_i}{\partial t} = \nu \mathrm{e}^{-\beta Q_b} \sum_{j \in N_i} \left[x_j \mathrm{e}^{c\beta(\mu_j - \mu_i)} - x_i \mathrm{e}^{c\beta(\mu_i - \mu_j)} \right]. \tag{22}$$

Using this equation for DMD-M-1.0 in addition to disabling hydrogen-hydrogen interactions in the potential evaluation for the most relevant first 0.6 ns allows to isolate the influence of kinetic self-interaction. Figure 7 shows no significant additional influence on the MSD over the entire time range, indicating that the self-interaction error is dominated by potential energy term.

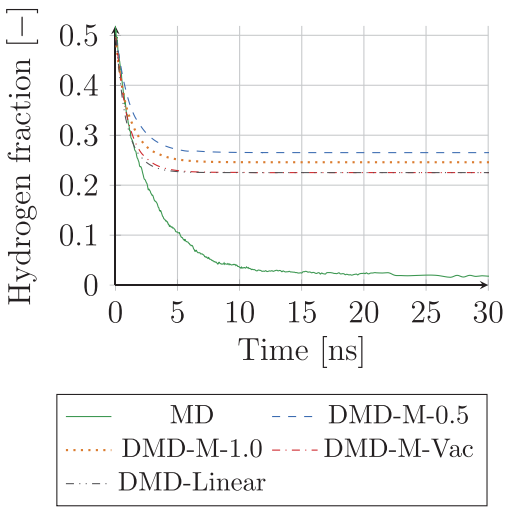

Figure 8. Hydrogen fraction in the inner half of the volume of the nanowire with average concentration of 0.2 as function of time for different simulation methods

4.2. Surface segregation in periodic cylindrical nanowires

4.2.1. Set-up

Segregation to surfaces and lattice defects represents a key application of DMD [8, 9, 40, 44]. The capability to capture these phenomena is tested for the case of surface segregation in palladium hydride nanowires with initial homogeneous hydrogen concentrations of 0.2 and 0.6. The study utilized cylindrical palladium hydride samples with a diameter of 10 nm and an axial length of 6 unit cells oriented in the ⟨100⟩-direction, which were constructed using the lattice constants determined in section 3. Periodic boundary conditions were applied in axial directions. Random hydrogen atoms were removed for MD samples to achieve the target average concentration and all hydrogen sites were initialized to this concentration for DMD samples. The resulting MD samples comprise 14 177 and 17 174 atoms for concentrations of 0.2 and 0.6, respectively, while the DMD samples contain 23 628 and 21 468 atom sites.

The MD simulations were conducted for 500 ns with a 1.0 fs time step using an NPT ensemble at 300 K to maintain zero average stress in the axial direction. The DMD samples were simulated according to the algorithm described in section 2.3.1 with the four kinetic equations introduced in section 2.2 and the same calibration as in the previous subsection for at least 125 ns as no significant changes were observed beyond 100 ns. The wire length was continuously adjusted during the DMD simulations to maintain zero axial stress.

4.2.2. Results

4.2.2.1. Concentration 0.2

All simulation methods unveil the same general behavior: due to the short sample length, there is no noticeable diffusion in axial direction and hydrogen diffuses in an approximately rotationally symmetrical diffusion pattern from the center of the wire towards the surface. This behavior allows to track the diffusion by monitoring the amount of hydrogen in the center of the nanowire. Figure 8 illustrates the temporal evolution of the hydrogen fraction within the inner half of the wire's volume. The initial fraction of approximately 0.5 decreases as hydrogen diffuses toward the surface, reaching equilibrium within 25 ns. All used simulation methods show a similar behavior during the first nanosecond. Subsequently, DMD simulations achieve equilibrium more rapidly and maintain a higher hydrogen fraction in the wire's center compared to the MD reference solution, where the central region becomes almost depleted of hydrogen. This distinction is also evident in the final radial distribution of hydrogen density shown in figure 9. All DMD implementations yield nearly identical radial distributions with notably higher central hydrogen density compared to MD.

To facilitate the comparison of the hydrogen distribution, DMD results were transformed into equivalent MD microstates by choosing location and occupation of each atom site based the respective probability distribution. Figure 10 displays the final hydrogen atom locations in the wire's cross-section after approximately 500 ns for both MD results and the DMD-M-0.5 implementation, which is representative of all used kinetic equations due to their similar distributions. Due to the lattice structure and six-unit-cell axial sample length, six octahedral sites share similar positions when projected to the cross

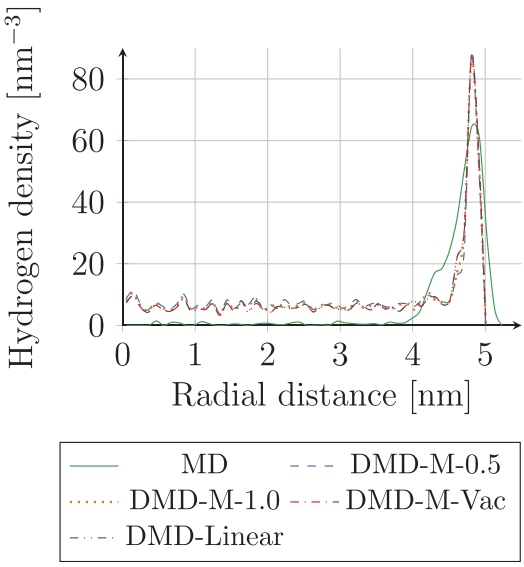

Figure 9. Hydrogen density as function of radial distance from the wire axis in the final state of the nanowire with average concentration of 0.2 for different simulation methods.

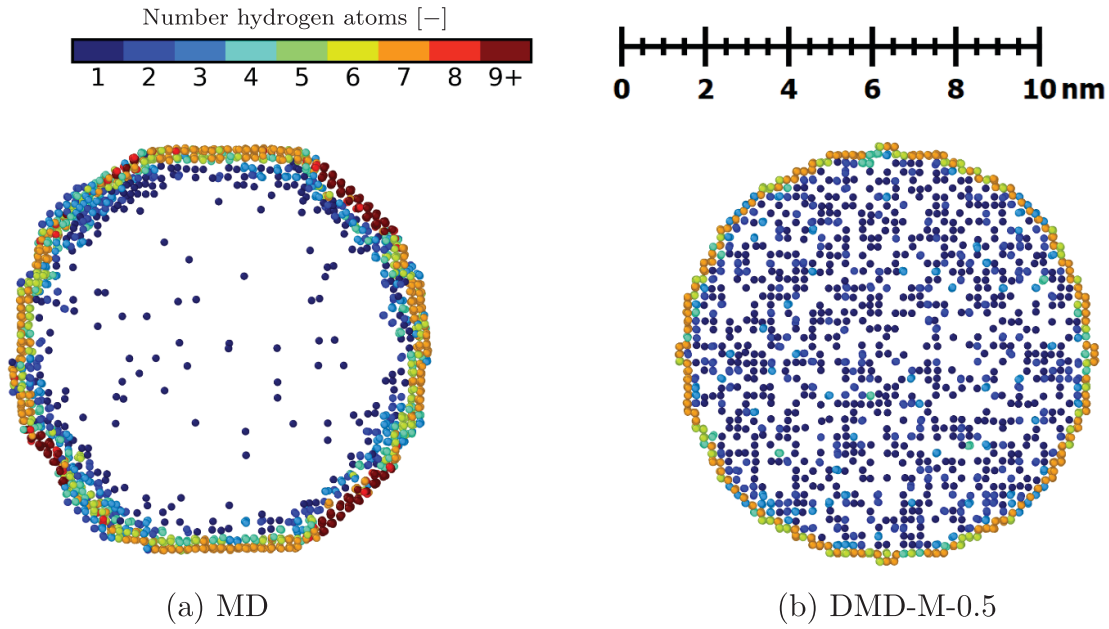

Figure 10. Cross-sectional visualization of location of hydrogen atoms in a palladium hydride nanowire with initial hydrogen concentration of 0.2 after 500 ns for (a) MD and (b) DMD (DMD-M-0.5) simulations. DMD results are transformed into an MD-equivalent microstate by stochastically sampling atom positions and occupations from their respective probability distributions. Colors indicate the number of hydrogen atoms within a 1 Å-radius cylinder in axial direction around the respective atom, revealing the effective hydrogen occupation when multiple octahedral sites share similar projected positions due to the six-unit-cell periodic structure.

section. To discern how many of those sites are occupied, hydrogen atoms are colored based on the amount of hydrogen within a 1 Å radius cylinder in axial direction around the atom. Ovito was utilized for visualization [31].

Both methods demonstrate predominately occupied surface sites, indicated by full occupation of all six octahedral sites in the same line of sight. However, figure 10 reveals higher central hydrogen retention in DMD simulations, while MD predicts almost complete surface and subsurface segregation. The MD results additionally exhibit palladium lattice restructuring at the surface, evident from the hydrogen atom arrangement in figure 10(a). This restructuring reduces surface energy through step reduction and enables higher hydrogen density through lattice rearrangement in $\langle 110 \rangle$ and $\langle 1\bar{1}0 \rangle$ directions, visible in the figure's red areas. Such restructuring is absent in DMD simulations.

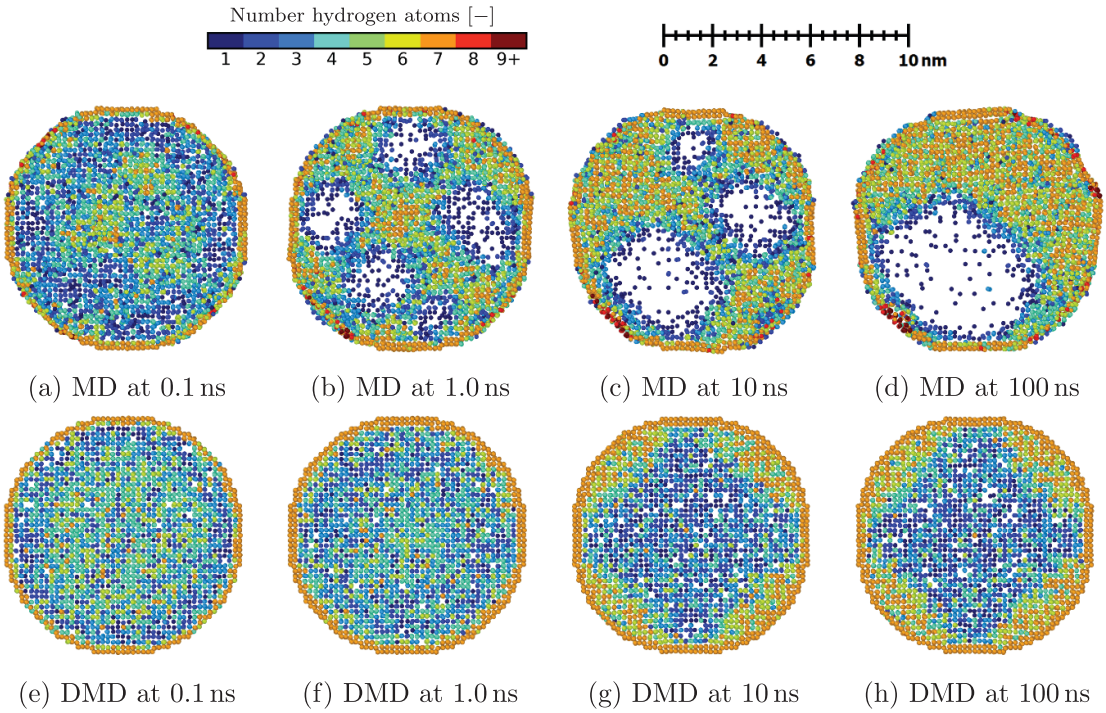

Figure 11. Cross-sectional location of hydrogen atoms in the palladium hydride nanowire with initial hydrogen concentration of 0.6 comparing MD and DMD-M-Vac simulations at 0.1 ns, 1 ns, 10 ns, and 100 ns. Cross-sectional visualization follows the method described in figure 10.

4.2.2.2. Concentration 0.6

Similar to the case with lower initial concentration, the nanowire with initial concentration of 0.6 also shows no significant diffusion in axial direction and can be reduced to the behavior in the cross section. Figure 11 illustrates hydrogen atom locations in the cross section at various time points for MD and DMD-M-Vac simulations, utilizing the same visualization methods as figure 10.

The MD simulation shows rapid surface diffusion within 0.1 ns, resulting in high surface and partial subsurface site occupation. Within 1 ns, distinct low-hydrogen α-PdH regions form, surrounded by β-PdH with well-defined boundaries. These regions consolidate over 100 ns into a single larger α-PdH region enclosed by β-PdH, maintaining stability for the subsequent 400 ns.

The results with DMD-M-Vac demonstrate similar initial surface and subsurface diffusion within 0.1 ns, achieving complete occupation of these sites by 1 ns. By 10 ns, the system reaches a stable state characterized by high hydrogen concentration regions along $\langle 110 \rangle$ and $\langle 1\bar{1}0 \rangle$ directions. However, phase distinction is less pronounced than in MD, with elevated hydrogen concentration in the α-phase. Unlike MD, DMD-M-Vac maintains symmetry with respect to (100), (010), (110), and $(1\bar{1}0)$ planes and high hydrogen regions do not consolidate. The other used kinetic equations exhibit similar general behavior and only their final states are shown in figure 12. All kinetic equations demonstrate hydrogen segregation favoring $\langle 110 \rangle$ and $\langle 1\bar{1}0 \rangle$ surface directions, with varying segregation intensities. DMD-M-Vac and DMD-Linear show the strongest segregation, while DMD-M-1.0 and particularly DMD-M-0.5 exhibit almost no phase separation.

The depiction of hydrogen fraction within the inner half of the wire's volume in figure 13 confirms these observations, showing rapid central hydrogen depletion until equilibrium for all kinetic equations. The equilibrium states maintain higher hydrogen content compared to the MD reference, despite the presence of hydrogen-rich β-PdH near the center in the MD solution. Consistent with figure 12, DMD-Linear and DMD-M-Vac behave similarly with the lowest central hydrogen retention, while DMD-M-1.0 and DMD-M-0.5 maintain higher central concentrations, with DMD-M-0.5 showing the highest values.

4.2.3. Discussion

While all used DMD kinetic equations successfully reproduce the general surface segregation patterns observed in the MD reference solutions, there are several key differences: DMD overestimates the hydrogen content in α-PdH and fails to capture surface restructuring for the low concentration case. For the

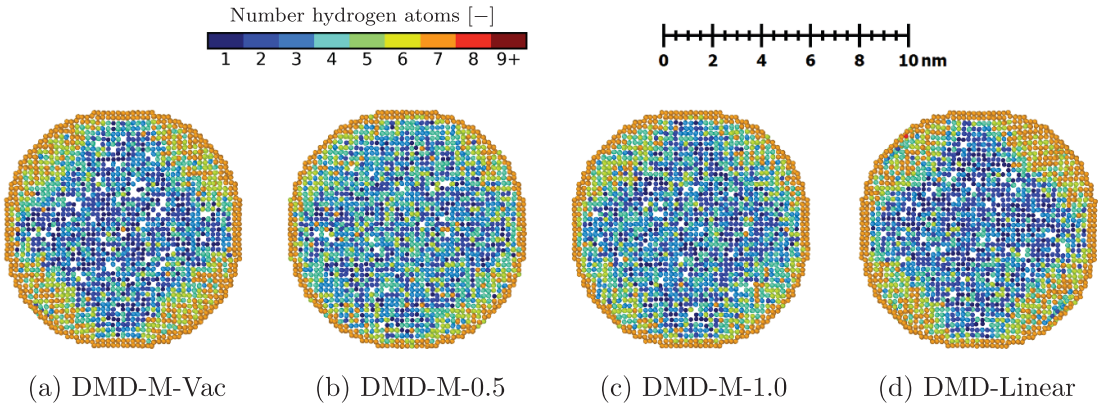

Figure 12. Final cross-sectional location of hydrogen atoms in the palladium hydride nanowire with initial hydrogen concentration of 0.6 for DMD simulations comparing the different kinetic equations. Cross-sectional visualization follows the method described in figure 10

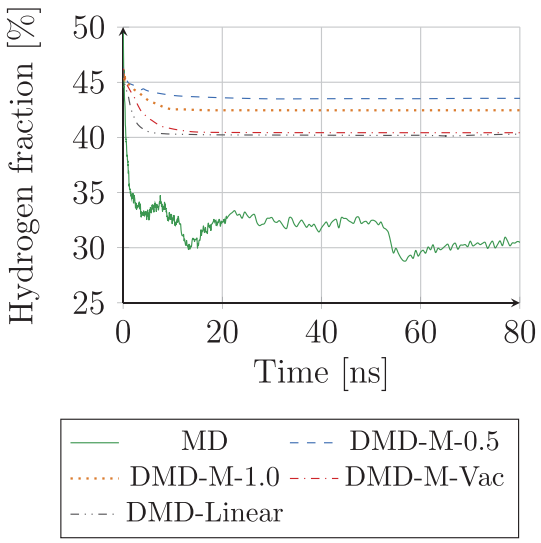

Figure 13. Development of the hydrogen fraction located in the center half of the volume of the nanowire with an average concentration of 0.6 based on the MD simulations and DMD simulations with different kinetic equations

high concentration case, DMD additionally shows less pronounced phase separation and incomplete phase consolidation.

The absence of surface restructuring stems from current DMD implementations' optimization approach, including the version used in this work [19]. When minimizing equation (11) for lattice relaxation, these implementations explore only the nearest energy minimum, neglecting configurations beyond local minima. Consequently, DMD relaxation cannot overcome energy barriers necessary for surface restructuring, preserving the initial palladium lattice structure. While more sophisticated optimization approaches beyond local minima could overcome this problem, they also pose the risk of conflicting with the concept of local equilibrium by including diffusive restructuring, e.g. by reordering of hydrogen sites. This limitation extends beyond mere structural changes, as surface restructuring modifies both the number and characteristics of available interstitial sites, presenting an inherent challenge for DMD simulation due to its requirement for available atom sites to facilitate diffusion. While additional empty sites can theoretically accommodate diffusion in regions with uncertain site characteristics [17], this approach would introduce practical challenges associated with initially unknown site positioning and challenging optimization of empty sites due to their minimal contribution to the functional in equation (11).

The most significant discrepancy between MD and DMD results is the less pronounced phase separation and lack of phase consolidation. Those deviations originate from three interconnected factors: First, the approximations discussed in section 3.3 directly influence the chemical potential. The differences in lattice and elastic constants documented in section 3 additionally influence the chemical potential indirectly due to lattice deformation and stress, e.g. through lattice mismatch and resulting stress in

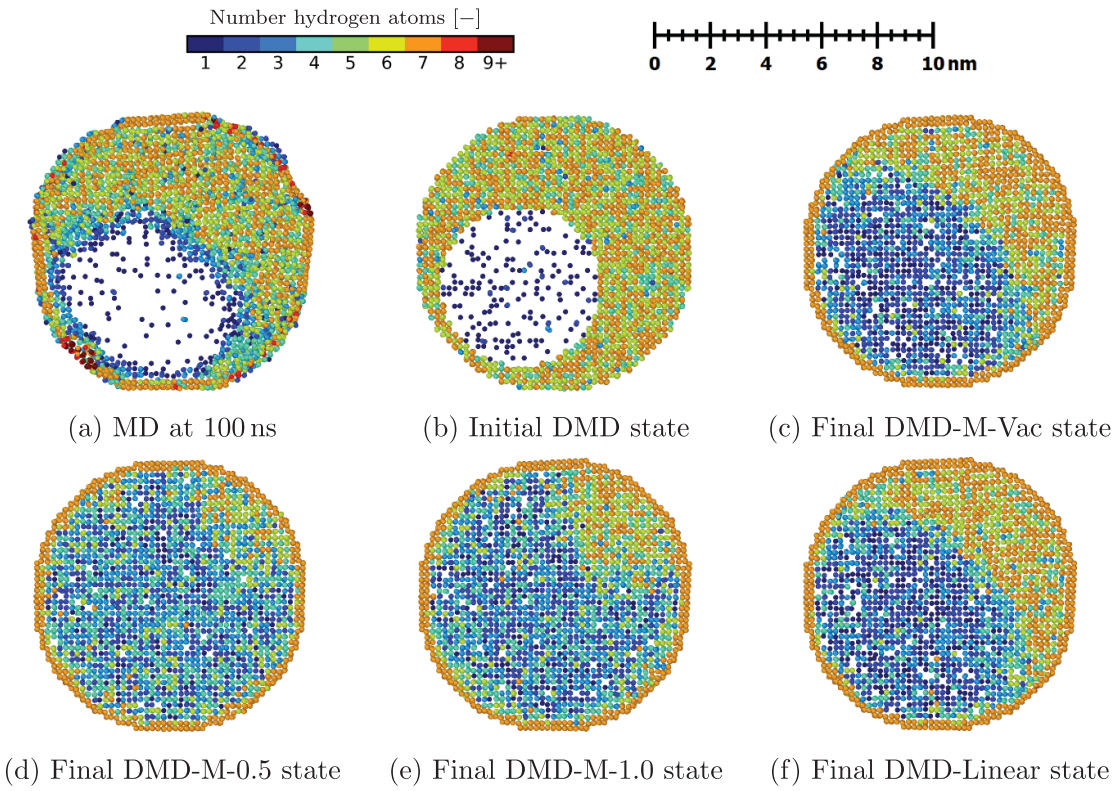

Figure 14. Cross-sectional location of hydrogen atoms in a palladium hydride nanowire following the visualization method described in figure 10. (a) Final state of MD simulations for the nanowire with 0.6 concentration (b) Initial state of DMD simulations chosen to approximate this final MD state. (c)–(f) Final stable state of DMD simulations with different kinetic equations based on this initial state

coexisting phases and their interface. As the chemical potential is the driving force of the diffusion, those influences have a strong impact on the kinetic behavior and final stable state. Second, the used kinetic equation directly determines possible stable states through its zeros, which depends on both the chemical potential difference and local concentration. Lastly, the deterministic integration of kinetic equations restricts diffusion towards the nearest minimum path, eliminating the random fluctuations present in MD that enable exploration of alternative minima.

To investigate the impact of deterministic integration, additional DMD simulations were conducted using an alternative initial hydrogen distribution approximating the final MD state. These simulations initialized the wire with a concentration of 0.87 except for a cylindrical region (radius 2.85 nm) corresponding to the MD simulation's α-phase location, where concentration was set to 0.05. This initial configuration has a average concentration of 0.603 and contains the sharp phase separation observed in the MD results. DMD simulations were conducted until a stable state is reached. The results, shown in figure 14, reveal that each DMD simulation converges to a stable state featuring a single β-phase region opposite the initial α-phase position, contrasting with the multiple β-phase regions seen in figure 12. This behavior confirms that the kinetic model prevents systems from overcoming unfavorable intermediate configurations, thereby inhibiting the phase consolidation observed in MD. However, the higher hydrogen content in the α-phase compared to MD indicates that approximations in chemical potential determination and kinetic equation zeros also contribute substantially to the observed differences.

Among the four kinetic equations examined, DMD-Linear and DMD-M-Vac demonstrate similar performance characteristics and provide the closest match with the MD reference solutions as observed by the lowest central hydrogen retention and sharpest phase separation. DMD-M-1.0 and DMD-M-0.5 only show a very weak phase separation and the highest hydrogen retention and are therefore the least suitable for this use case.

4.3. Nanocube hydration

4.3.1. Simulation setup

The hydration of a palladium nanocube with a side length of 10 unit cells serves as a final validation case, representing a typical DMD application [32–36]. To simulate the hydration with MD, a designated

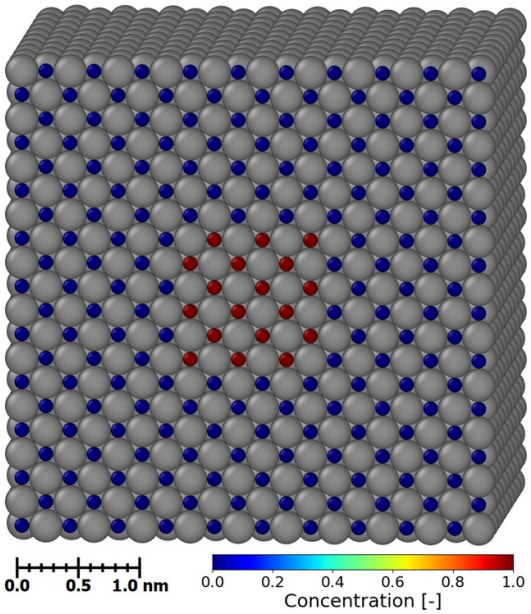

Figure 15. Initial configuration of the nanocube. Palladium atoms are depicted in grey and hydrogen atoms are colored based on their initial concentration

surface area functioned as an hydrogen inflow region. The octahedral interstitial surface sites within this area were tracked based on the mean position of the surrounding palladium atoms. Hydrogen atoms were inserted into vacant inflow sites every 50 fs, resulting in an average concentration of 0.99995 for inflow sites. The DMD simulations replicated these conditions by constraining the concentration of corresponding sites to 0.99995. All other octahedral interstitial sites were initially empty, i.e. no hydrogen atoms present for MD simulations and empty hydrogen sites for DMD simulations.

While theoretical considerations and experimental observations predict hydration initiation at the nanocube corners, limitations of this used MD algorithm necessitated a modified approach. Corner regions exhibit insufficient lattice stability for reliable interstitial site tracking due to variable site numbers and changing neighbor configurations. Therefore, the inflow region was positioned at the center of one face of the cube, where the palladium lattice maintained sufficient stability for consistent surface site tracking. Although this configuration may not fully represent actual palladium nanocube hydration processes, it enables direct comparison between MD and DMD under identical conditions for relevant a hydration process. Figure 15 illustrates the initial DMD configuration.

The MD simulation employed an NVT ensemble and proceeded for 170 ns with 1 fs time step, terminating when surface restructuring prevents reliable hydrogen atom placement. The DMD simulations utilizing the four kinetic equations detailed in section 2.2 were conducted for 200 ns. DMD-Linear was stopped after 85 ns as it reached convergence to a final stable state.

4.3.2. Results

Figure 16(a) shows the temporal development of the cube's hydrogen content, revealing distinct phases in hydrogen uptake dynamics of the MD reference solution: a rapid hydrogen absorption during the initial 2.5 ns until reaching a hydrogen content of approximately 1000 atoms, followed by a slower intake thereafter. DMD-Linear accurately reproduces the initial rapid uptake phase but maintains this elevated absorption rate until reaching over 2000 atoms, after which it converges towards a stable level of hydrogen content. DMD-M-0.5 and DMD-M-1.0 demonstrate similar behavior but with moderately reduced initial uptake rates and higher stabilization thresholds, with DMD-M-1.0 exhibiting earlier rate reduction. DMD-M-Vac displays the slowest hydrogen intake profile and the absorption slows down at the lowest hydrogen content.

The average occupation of surface, subsurface (defined as one layer below the surface) and bulk sites, calculated by categorizing hydrogen sites based on palladium neighbors and theoretical site count in an undeformed cube, provides additional insight in the hydration dynamics. Figures 16(b)–(d) demonstrate that MD simulations exhibit rapid initial hydration dominated by surface diffusion until surface site saturation, followed by approximately linear occupation of subsurface sites and gradually increasing bulk occupation. The average surface occupation surpassing 1.0 can be attributed to moderate surface

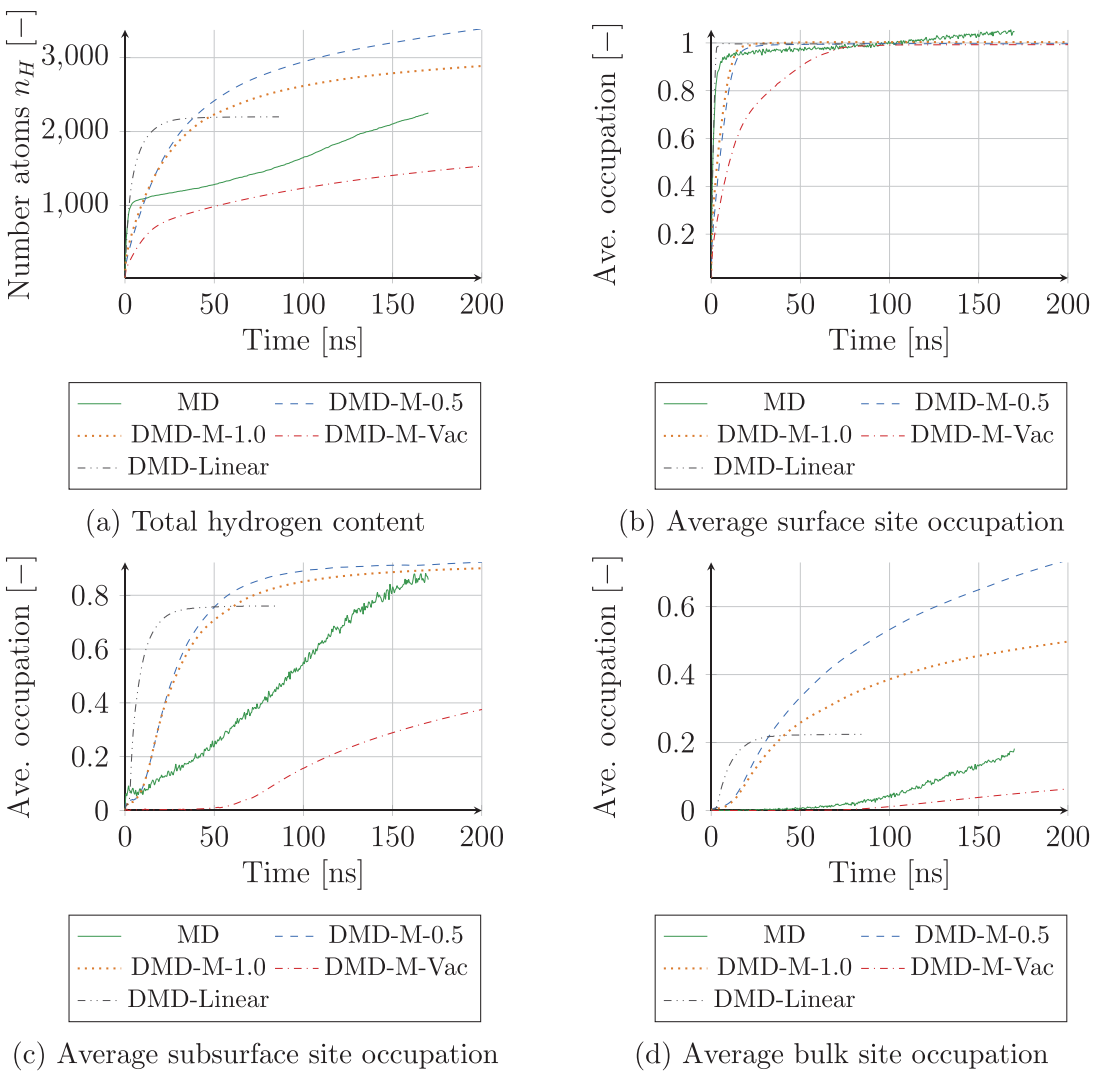

Figure 16. Temporal development of the hydration of the palladium nanocube based on total hydrogen content (a) and the average occupation of surface (b), subsurface (c) and bulk (d) sites.

restructuring, e.g. at corners, creating additional sites. All kinetic equations except DMD-M-Vac accurately reproduce the rapid surface site occupation but overestimate the intake to subsurface and especially bulk sites. The rate of surface site occupation using DMD-M-Vac is noticeably slower. However, similar to MD and unlike the other kinetic equations, it only shows occupation of subsurface sites and gradually increasing bulk diffusion once almost all surface sites are occupied, but with reduced hydration speed across all site types.

Figure 17 displaying the hydrogen atom locations in a central 8-unit-cell slice of the nanocube at different amounts of hydrogen intake corroborates these findings. The slice thickness excludes surface unit cells to enhance visualization of internal processes. The visualization approach is identical to figure 10 with an hydrogen number of 8 indicating full occupation of interstitial sites due to the slice thickness. Comparison points are selected at approximately 500, 1000, and 2000 absorbed hydrogen atoms to normalize for varying diffusion rates of the methods. Figures 17(a), (f) and (k) confirm that during rapid uptake, MD simulations show preferential surface site occupation, followed by subsurface penetration and limited bulk diffusion. DMD-M-Vac most accurately reproduces this behavior, as evidenced in figures 17(b), (g) and (l), though with increased bulk occupation once surface sites are filled. DMD-Linear exhibits premature subsurface and bulk occupation near the inflow region (figures 17(e) and (j)) while maintaining reasonable overall behavior. DMD-M-0.5 and DMD-M-1.0 show the same early-stage deviations as DMD-Linear, yet more pronounced.

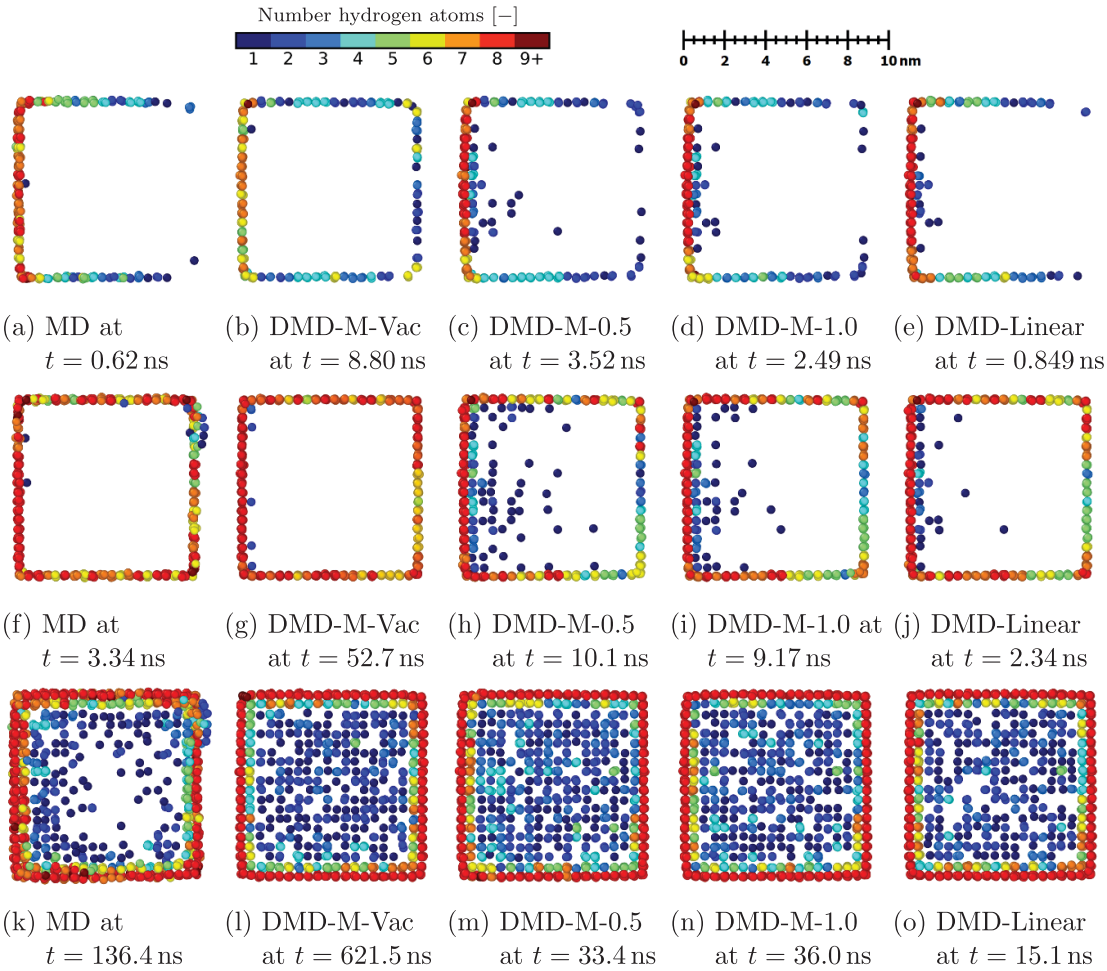

Figure 17. Position of hydrogen atoms in a central 8-unit-cell slice of the nano cube at different times for the different simulation methods. The times are chosen based on the accumulated hydrogen inflow n_H, where the first row is at $n_H \approx 500$, the second at $n_H \approx 1000$ and the third at $n_H \approx 2000$. Cross-sectional visualization follows the method described in figure 10

4.3.3. Discussion

This case study encompasses both surface and bulk diffusion processes, characterized by distinct diffusion pathways and energy barriers, leading to increased surface diffusion speed. Additionally, surface sites are energetically favorable as observed by the surface segregation of the previous example. Together, this manifests in the MD simulations as markedly reduced hydrogen uptake following surface site saturation. While DMD implementations can theoretically accommodate environment-dependent coefficients in equations (12) and (14), only few and limited studies implement this capability [17]. Recent developments enable to consider this through on-the-fly calculations of attempt frequencies and energy barriers [20], which is however not considered in this work. The used approach employs uniform coefficients based on bulk diffusion characteristics, suggesting that incorporating environment-dependent coefficients would accelerate surface diffusion and early-stage uptake. Paradoxically, DMD-M-0.5, DMD-M-1.0, and DMD-Linear already match early-stage uptake through surface site occupation reasonably well and overestimate uptake rates to subsurface and bulk sites.

One significant factor to the behavior of those kinetic equations is the configurational entropy contribution to the chemical potential. As concentrations approach limiting values, this contribution becomes unbounded, requiring artificial constraints for numerical stability. Kinetic equations incorporating configurational entropy exhibit high sensitivity to these constraints and pre-described inflow concentrations, leading to overestimated diffusion rates and increased jump rates from high concentration surface sites to subsurface and bulk sites. DMD-M-Vac, which is independent of configurational entropy contributions, demonstrates reduced sensitivity to inflow conditions and exhibits slower initial uptake than MD during surface-dominated diffusion. This suggests potential for improved agreement with the MD reference solution when accounting for higher surface diffusion rates through environment dependent Q_{bij}, which would lead to faster surface site occupation and subsequently earlier onset of subsurface occupation. This indicates DMD-M-Vac as the most promising implementation for this case study.

5. Conclusion

This study presents a systematic comparison between DMD simulations, utilizing various kinetic equations, and MD reference solutions for both static properties and diffusive processes in palladium hydride. This approach offers distinct advantages over experimental validation by isolating intrinsic DMD methodological errors from those arising from interatomic potential choices and general model assumptions like boundary conditions, which is particularly valuable for diffusive processes, where existing DMD validation remains limited.

The results demonstrate that DMD accurately reproduces MD-calculated lattice constants, though deviations grow with temperature and hydrogen concentration. Elastic constant calculations show excellent agreement with MD at near-zero temperatures, but errors increase substantially at 300 K, particularly at elevated hydrogen concentrations, reaching magnitudes comparable to the calculated values themselves. Additionally, the crystal symmetry and used numerical integration method magnify small discontinuities in the used EAM potential leading to discontinuities in the DMD-calculated elastic constants not observed for MD.

For single hydrogen atom diffusion in palladium lattice, all tested kinetic equations successfully reproduce long-term behavior predicted by analytical and MD reference solutions, yet exhibit initial deviations arising from the used calibration approach at small chemical potential gradients, while the analytical solution is only valid after sufficient time. Simulations of nanowire surface segregation and nanocube hydration reveal that DMD qualitatively captures general trends from MD simulations but exhibits significant quantitative differences. Notable discrepancies include hydrogen content predictions in α-PdH, inability to reproduce phase consolidation dynamics observed in nanowire simulations and mismatches in the hydration rate for the nanocube. Among the tested kinetic equations, DMD-M-Vac and DMD-Linear demonstrate superior performance for the use case of palladium hydride. The hydrogen uptake rate to different type of interstitial sites of the nanocube identifies DMD-M-Vac as the most promising candidates for further refinement through incorporation of local energy barrier effects.

The present results demonstrate that the applicability of DMD is strongly problem-dependent. Nevertheless, its potential for substantial computational speed-up only limited by the fastest diffusive processes and streamlined input requirements limited to an interatomic potential and diffusive constants motivate continued methodological refinement and systematic benchmarking against established time-bridging alternatives. The numerical examples identify local constants for kinetic equation coefficients, inability to model phase nucleation, correlated vibrations and third-order Gaussian–Hermite quadrature as key drivers of DMD accuracy. Consequently, improved integration schemes and more sophisticated coefficient selection represent critical avenues for future research. Even though self-interaction between partially occupied sites did not show a strong impact on the reported results, this observation requires validation across diverse crystal systems where diffusing species may play a more dominant role.

While the current study provides new insights into the intrinsic DMD error, it focuses on samples up to 10 nm. Studies specifically designed for phenomena only occurring in larger samples like dislocation nucleation could provide insight on the usability of DMD in such cases. Furthermore, the fast diffusion speed allowing a direct comparison between MD and DMD also prohibits a meaningful computational efficiency comparison. DMD is designed for significantly slower processes with larger time steps, especially since conservative time steps were chosen to prioritize result validity. DMD time steps are frequently constrained by sites with near-limit concentrations, complicating direct performance comparisons as a single ill-placed site can determine overall performance. Lastly, studies for substitutional diffusion are required to determine if the observed performance of the kinetic equations is transferable.

In conclusion, the present comparison between MD and DMD simulations for various diffusive processes in palladium hydride spanning from single atom diffusion to complex hydration processes validates DMD's ability to reproduce general observed trends, while unveiling several quantitative discrepancies not observed before. Additionally, this comparison highlights the potential of this use case as possible benchmark system for the validation of further accelerated atomistic simulation methods.

Acknowledgments

We thank Prof. Mauricio Ponga for providing early access to their code, which we used in this work. We are also grateful to Prof. Michael Ortiz for sharing their in-house code during the development of this project.

Data availability statement

The data cannot be made publicly available because the volume and structure of the raw files make preparation and hosting prohibitively time-consuming and costly within the scope of this project. The data that support the findings of this study are available upon reasonable request from the authors.

Appendix. Calibration of kinetic equations

The master equation can be calibrated by matching its long-wavelength limit to the macroscopic advection-diffusion equation for bulk diffusion. Using equation (1), the trial phase average of the occupation n_i can be calculated as

$$\langle n_i \rangle_0 = x_i = \frac{Z_i \mathrm{e}^{\beta\mu_i}}{1 + Z_i \mathrm{e}^{\beta\mu_i}} \tag{23}$$

with the shorthand

$$Z_i = \frac{1}{h^3} \int_\Gamma \exp\left(\frac{\beta_i}{2m_i} \left| \underline{\boldsymbol{p}}_i \right|^2 + \frac{m_i \beta_i {\omega_i}^2}{2} \left| \underline{\boldsymbol{q}}_i - \bar{\underline{\boldsymbol{q}}}_i \right|^2 \right) \mathrm{d}q\mathrm{d}p, \tag{24}$$

which can be solved for

$$\mathrm{e}^{\beta\mu_i} = \left(\frac{x_i}{Z_i \left(1 - x_i\right)} \right). \tag{25}$$

Substituting this into equation (15) results in

$$\frac{\partial x_i}{\partial t} = \nu \mathrm{e}^{-\beta Q_b} \sum_{j \in N_i} \left[\frac{Z_i^c}{Z_j^c} \frac{\left[x_j \left(1 - x_i\right)\right]^{c+1}}{\left[x_i \left(1 - x_j\right)\right]^c} - \frac{Z_j^c}{Z_i^c} \frac{\left[x_i \left(1 - x_j\right)\right]^{c+1}}{\left[x_j \left(1 - x_i\right)\right]^c} \right], \tag{26}$$

which depends only on the concentration and not the chemical potential. For bulk sites without influence of lattice defects, neighboring sites of the same species and with similar concentration have a comparable vibration frequency and therefore $Z_i \approx Z_j$, yielding

$$\frac{\partial x_i}{\partial t} \approx \nu \mathrm{e}^{-\beta Q_b} \sum_{j \in N_i} \left[\frac{\left[x_j \left(1 - x_i\right)\right]^{c+1}}{\left[x_i \left(1 - x_j\right)\right]^c} - \frac{\left[x_i \left(1 - x_j\right)\right]^{c+1}}{\left[x_j \left(1 - x_i\right)\right]^c} \right] \tag{27}$$

as approximation of equation (26). Linearizing this equation in x_j around x_i yields

$$\frac{\partial x_i}{\partial t} \approx (2c+1)\, \nu \mathrm{e}^{-\beta Q_b} \sum_{j \in N_i} \left(x_j - x_i\right). \tag{28}$$

To match the behavior between the atomistic diffusion model and a continuum model, the continuous concentration field x is introduced. This allows to approximate the concentration x_j using a second order Taylor series around site i as

$$x_j \approx x_i + \nabla x(\underline{\boldsymbol{r}}_i) \cdot \underline{\boldsymbol{r}}_{ji} + \frac{1}{2} \nabla\nabla x(\underline{\boldsymbol{r}}_i) : \underline{\boldsymbol{r}}_{ji} \otimes \underline{\boldsymbol{r}}_{ji} \tag{29}$$

where ∇ is the Nabla operator, $\nabla x(\underline{\boldsymbol{r}}_i)$ and $\nabla\nabla x(\underline{\boldsymbol{r}}_i)$ are the gradient and Hessian matrix of x evaluated at the position $\underline{\boldsymbol{r}}_i$ of site i, respectively, and : and $\otimes$ notate the double contraction and tensor product. $\underline{\boldsymbol{r}}_{ji} = \underline{\boldsymbol{r}}_j - \underline{\boldsymbol{r}}_i$ represents the distance vector between site j and i. Introducing this Taylor series in equation (28) results in

$$\begin{aligned} \frac{\partial x_i}{\partial t} &\approx (2c+1)\, \nu \mathrm{e}^{-\beta Q_b} \sum_{j \in N_i} \left(\nabla x(\underline{\boldsymbol{r}}_i) \cdot \underline{\boldsymbol{r}}_{ji} + \frac{1}{2} \nabla\nabla x(\underline{\boldsymbol{r}}_i) : \underline{\boldsymbol{r}}_{ji} \otimes \underline{\boldsymbol{r}}_{ji} \right) \\ &= (2c+1)\, \nu \mathrm{e}^{-\beta Q_b} a_0^2 \nabla \cdot \nabla x(\underline{\boldsymbol{r}}_i), \end{aligned} \tag{30}$$

where the symmetry and the relative position of nearest neighbors in an FCC lattice is used for $\sum_{j\in N_i}\nabla x(\underline{\boldsymbol{r}}_i)\cdot\underline{\boldsymbol{r}}_{ji}=0$ and $\sum_{j\in N_i}\underline{\boldsymbol{r}}_{ji}\otimes\underline{\boldsymbol{r}}_{ji}=2a_0^2\underline{\underline{\boldsymbol{I}}}$ with identity tensor $\underline{\underline{\boldsymbol{I}}}$. Requiring this atomistic diffusion model to match the advection-diffusion equation

$$\frac{\partial x}{\partial t}=D_{\mathrm{H}}\nabla\cdot\nabla x-\underline{\boldsymbol{v}}\nabla x \tag{31}$$

with constant diffusion and zero divergence yields

$$\nu\mathrm{e}^{-\beta Q_b}=\frac{D_{\mathrm{H}}}{(2c+1)\,a_0^2} \tag{32}$$

as calibration equation for the master equation (equation (15)). The same principle can be followed for equation (16), yielding

$$\nu\mathrm{e}^{-\beta Q_b}=\frac{D_{\mathrm{H}}}{a_0^2}, \tag{33}$$

which is equivalent to the calibration used in [17].

ORCID iDs

Philipp M Schäfer 0009-0003-1418-0356
Christian J Cyron 0000-0001-8264-0885

References

[1] Adams B D and Chen A 2011 The role of palladium in a hydrogen economy *Mater. Today* **14** 282–9
[2] Alí M, Crespo E, Ruda M, Bringa E and Ramos S 2020 Hydrogen effects on the mechanical properties of nanocrystalline free-standing palladium thin films *Int. J. Hydrog. Energy* **45** 15213–25
[3] Baker K L and Curtin W A 2015 Assessment of phase-field-crystal concepts using long-time molecular dynamics *Phys. Rev. B* **91** 014103
[4] Baldi A, Narayan T C, Koh A L and Dionne J A 2014 In situ detection of hydrogen-induced phase transitions in individual palladium nanocrystals *Nat. Mater.* **13** 1143–8
[5] Balluffi R W, Allen S M and Carter W C 2005 *Kinetics of Materials* (Wiley) (https://doi.org/10.1002/0471749311)
[6] Crespo E A, Ruda M, de Debiaggi S R, Bringa E M, Braschi F U and Bertolino G 2012 Hydrogen absorption in Pd nanoparticles of different shapes *Int. J. Hydrog. Energy* **37** 14831–7
[7] de Debiaggi R S, Crespo E, Braschi F, Bringa E, Alí M and Ruda M 2014 Hydrogen absorption in Pd thin-films *Int. J. Hydrog. Energy* **39** 8590–5
[8] Dontsova E, Rottler J and Sinclair C W 2014 Solute-defect interactions in Al-Mg alloys from diffusive variational Gaussian calculations *Phys. Rev. B* **90** 174102
[9] Dontsova E, Rottler J and Sinclair C W 2015 Solute segregation kinetics and dislocation depinning in a binary alloy *Phys. Rev. B* **91** 224103
[10] Farmer B, Luskin M, Plecháč P and Simpson G 2017 Spin-diffusions and diffusive molecular dynamics *Modelling Simul. Mater. Sci. Eng.* **25** 084003
[11] Frenkel D and Smit B 2023 *Understanding Molecular Simulation: From Algorithms to Applications* (Elsevier) (https://doi.org/10.1016/B978-0-12-267351-1.X5000-7)
[12] Gonzalez-Ferreiro B, Romero I and Ortiz M 2016 A numerical method for the time coarsening of transport processes at the atomistic scale *Modelling Simul. Mater. Sci. Eng.* **24** 045011
[13] Gupta P, Ortiz M and Kochmann D M 2021 Nonequilibrium thermomechanics of Gaussian phase packet crystals: application to the quasistatic quasicontinuum method *J. Mech. Phys. Solids* **153** 104495
[14] Hirel P 2015 Atomsk: a tool for manipulating and converting atomic data files *Comput. Phys. Commun.* **197** 212–9
[15] Hsu D K and Leisure R G 1979 Elastic constants of palladium and β-phase palladium hydride between 4 and 300 K *Phys. Rev. B* **20** 1339–44
[16] Li G *et al* 2014 Hydrogen storage in Pd nanocrystals covered with a metal–organic framework *Nat. Mater.* **13** 802–6
[17] Li J, Sarkar S, Cox W T, Lenosky T J, Bitzek E and Wang Y 2011 Diffusive molecular dynamics and its application to nanoindentation and sintering *Phys. Rev. B* **84** 054103
[18] Mendez J, Ponga M and Ortiz M 2018 Diffusive molecular dynamics simulations of lithiation of silicon nanopillars *J. Mech. Phys. Solids* **115** 123–41
[19] Mendez J P and Ponga M 2021 MXE: a package for simulating long-term diffusive mass transport phenomena in nanoscale systems *Comput. Phys. Commun.* **260** 107315
[20] Molinos M, Ortiz M and Ariza M 2025 On-the-fly meanfield transition-state theory for diffusive molecular dynamics *Mech. Mater.* **207** 105380
[21] Narayan T C, Hayee F, Baldi A, Koh A L, Sinclair R and Dionne J A 2017 Direct visualization of hydrogen absorption dynamics in individual palladium nanoparticles *Nat. Commun.* **8** 1–8
[22] Perez D, Uberuaga B P, Shim Y, Amar J G and Voter A F 2009 *Chapter 4 Accelerated Molecular Dynamics Methods: Introduction and Recent Developments* (Elsevier) pp 79–98
[23] Ponga M and Sun D 2018 A unified framework for heat and mass transport at the atomic scale *Modelling Simul. Mater. Sci. Eng.* **26** 035014

[24] Radhakrishnan B, Gorti S B, Nicholson D M and Dantzig J 2012 Comparison of phase field crystal and molecular dynamics simulations for a shrinking grain *J. Phys.: Conf. Ser.* **402** 012043
[25] Ruda M, Crespo E and de Debiaggi S R 2010 Atomistic modeling of H absorption in Pd nanoparticles *J. Alloys Compd.* **495** 471–5
[26] Safarik D J, Schwarz R B, Paglieri S N, Quintana R L, Tuggle D and Byler D D 2010 Composition dependence of the elastic constants of β-phase and (α+β)-phase PdHx *Ultrasonics* **50** 155–60
[27] Sarkar S, Li J, Cox W T, Bitzek E, Lenosky T J and Wang Y 2012 Finding activation pathway of coupled displacive-diffusional defect processes in atomistics: dislocation climb in fcc copper *Phys. Rev. B* **86** 014115
[28] Saxena S, Bastek J-H, Spinola M, Gupta P and Kochmann D M 2023 GNN-assisted phase space integration with application to atomistics *Mech. Mater.* **182** 104681
[29] Schwarz R, Bach H, Harms U and Tuggle D 2005 Elastic properties of Pd–hydrogen, Pd–deuterium and Pd–tritium single crystals *Acta Mater.* **53** 569–80
[30] Simpson G, Luskin M and Srolovitz D J 2016 A theoretical examination of diffusive molecular dynamics *SIAM J. Appl. Math.* **76** 2175–95
[31] Stukowski A 2009 Visualization and analysis of atomistic simulation data with OVITO–the open visualization tool *Modelling Simul. Mater. Sci. Eng.* **18** 015012
[32] Sun X 2024 Exploring solute-defect interactions in nanosized palladium hydrides across multiple time scales *Comput. Mater. Sci.* **231** 112582
[33] Sun X and Jin R 2024 Size and shape dependence of hydrogen-induced phase transformation and sorption hysteresis in palladium nanoparticles *Modelling Simul. Mater. Sci. Eng.* **32** 085012
[34] Sun X, Ariza M, Ortiz M and Wang K 2017 Acceleration of diffusive molecular dynamics simulations through mean field approximation and subcycling time integration *J. Comput. Phys.* **350** 470–92
[35] Sun X, Ariza P, Ortiz M and Wang K G 2018 Long-term atomistic simulation of hydrogen absorption in palladium nanocubes using a diffusive molecular dynamics method *Int. J. Hydrog. Energy* **43** 5657–67
[36] Sun X, Ariza M, Ortiz M and Wang K 2019 Atomistic modeling and analysis of hydride phase transformation in palladium nanoparticles *J. Mech. Phys. Solids* **125** 360–83
[37] Thompson A P *et al* 2022 LAMMPS-a flexible simulation tool for particle-based materials modeling at the atomic, meso and continuum scales *Comput. Phys. Commun.* **271** 108171
[38] Ulvestad A *et al* 2015 Avalanching strain dynamics during the hydriding phase transformation in individual palladium nanoparticles *Nat. Commun.* **6** 1–8
[39] Ulvestad A *et al* 2017 Three-dimensional imaging of dislocation dynamics during the hydriding phase transformation *Nat. Mater.* **16** 565–71
[40] Venturini G, Wang K, Romero I, Ariza M and Ortiz M 2014 Atomistic long-term simulation of heat and mass transport *J. Mech. Phys. Solids* **73** 242–68
[41] Voter A F 2007 *Introduction to the Kinetic Monte Carlo Method* (Springer) pp 1–23
[42] Wang K, Ortiz M and Ariza M 2015 Long-term atomistic simulation of hydrogen diffusion in metals *Int. J. Hydrog. Energy* **40** 5353–8
[43] Weissmüller J and Lemier C 2000 On the size dependence of the critical point of nanoscale interstitial solid solutions *Phil. Mag. Lett.* **80** 411–8
[44] Zhang B, Guo Y, Liu Z, Li M, Shi D, Li Y, Song J, Bu M and Du S 2021 Atomic modeling of the segregation of vacancies on 111 dislocations in α-iron by diffusive molecular dynamics simulations *J. Alloys Compd.* **857** 157486
[45] Zhou X, Zimmerman J, Wong B and Hoyt J 2008 An embedded-atom method interatomic potential for Pd–H alloys *J. Mater. Res.* **23** 704–18
[46] Zhou X, Heo T, Wood B, Stavila V, Kang S and Allendorf M 2018 Temperature-and concentration-dependent hydrogen diffusivity in palladium from statistically-averaged molecular dynamics simulations *Scr. Mater.* **149** 103–7
[47] Zhou X W, Heo T W, Wood B C, Stavila V, Kang S and Allendorf M D 2018 Molecular dynamics studies of fundamental bulk properties of palladium hydrides for hydrogen storage *J. Appl. Phys.* **123** 225105